Erosion-driven changes in soil cation exchange capacity quantified using barium isotopes

Luke Bridgestock[1,2*], Emily Stevenson[1,$], J. Jotautas Baronas[1,3], Alasdair Knight[1,4], Harold J. Bradbury[1,5], Alexandra V. Turchyn[1] and Edward T. Tipper[1]

[1]Department of Earth Sciences, University of Cambridge, Downing Street, Cambridge, CB2 3EQ, UK

[2]School of Earth and Environmental Sciences, University of St Andrews, Bute Building, Queen's Terrace, St Andrews, KY16 9TS, UK

[3]Department of Earth Sciences, Durham University, Durham, DH1 3LE, County Durham, UK

[4]Department of Earth Sciences, University of Oxford, South Parks Road, Oxford, OX1 3AN, UK

[5]Department of Earth, Ocean and Atmospheric Sciences, University of British Columbia, Vancouver, British Columbia, Canada

[$] Now at GFZ Helmholtz-Zentrum für Geoforschung, 14473, Deutschland

*Corresponding author; ljb35@st-andrews.ac.uk

This paper is a non-peer reviewed preprint submitted to EarthArXiv. It has been submitted for peer review in the journal Geochimica et Cosmochimica Acta.

Abstract (288 words)

Human activities have perturbed the balance between rates of soil erosion and formation, driving declines in soil quality. However, quantifying these soil imbalances remains challenging, especially at large scales. Here we present a novel isotope mass balance approach that can be used to quantify river catchment wide rates of change in cation exchange capacity (CEC), a key soil quality metric, in response to erosional perturbations. The approach uses differences in Ba isotope composition between river export fluxes and chemical weathering inputs to solve for rates of change of Ba storage within upstream soil exchange pools. Accumulation of Ba within soil exchange pools, due increases in CEC, results in the preferential export of heavier Ba isotopes in river dissolved and erosional outputs. Data for river water and suspended particulate material (SPM) samples from the Irrawaddy and Salween river demonstrate the utility of the approach. The Ba isotopic data are used to quantify associated changes in catchment wide CEC. During peak discharge conditions the Salween River basin is balanced within uncertainty of the data for its catchment wide CEC budget. By contrast, the Irrawaddy River basin features net CEC accumulation of at least 35 ± 5 meq/m^2/year during peak discharge conditions. This net CEC accumulation in the Irrawaddy River basin is interpreted to reflect SPM deposition in floodplains, while the CEC balance observed in the Salween River basin likely reflects the lack of a significant floodplain area in this catchment. These results demonstrate the utility of this approach to place quantitative constraints on river catchment wide soil quality (CEC) changes driven by human perturbations to terrestrial sediment transport, including the reduction of SPM deposition in floodplains due to dam construction and accelerated soil erosion due to land-use and climate change.

Keywords: Barium isotopes; Critical zone; cation exchange capacity; land degradation; soil erosion

1. Introduction

Human activities that alter the erosion and redistribution of soils are recognized as a leading cause of land degradation (Montgomery, 2007, Li and Fang, 2016, Olsson et al., 2019, Syvitski et al., 2022). Land-use changes and agricultural practices accelerate soil erosion rates by one to two orders-of-magnitude (Montgomery, 2007). Changes in the hydrological cycle driven by anthropogenic climate change are predicted to further increase soil erosion rates in the coming century (Li and Fang, 2016). Conversely, human modification of hydrological networks, principally due to dam construction, are reducing the delivery of this eroded material to downstream depositional environments (Syvitski et al., 2022). These perturbations impact the sustainability of soil reserves by altering the balance between soil formation processes and soil loss/gain by erosion/deposition. In turn, these perturbations are a major driver of land degradation, defined as the negative trend in land condition due to direct and indirect human processes (Olsson et al., 2019).

Current approaches for assessing rates of land degradation associated with perturbations to the balance of soil erosion versus formation are based on comparing constraints on soil erosion rates to threshold values (soil loss tolerance) assumed to represent a sustainable balance with soil formation rates (Montgomery et al., 2007). However, the resulting bulk soil balances have at least an order-of-magnitude uncertainty due to difficulty of obtaining constraints on soil erosion and soil formation rates integrated over the same spatiotemporal scales (Montgomery, 2007, Garcia-Ruiz

et al., 2015). At a river catchment scale, the balances between erosion and deposition along sediment transport pathways further complicate comparisons to soil formation rate constraints. It is also unclear how bulk soil imbalances quantitatively link to changes in soil quality that underpin the associated land degradation. Changes to soil erosion differentially impact various soil particle size fractions, resulting in changes in soil composition. Secondary phases including organic matter and clay minerals, the products of soil formation processes, support key soil functions and tend to have finer grain sizes compared to primary minerals (Bouchez et al., 2011, Ćirić et al., 2023). These phases are more susceptible to erosional losses, but the complexity of hydrodynamic processes along sediment transport pathways obscures the link between bulk soil erosion and soil composition changes.

This study presents a new stable isotope mass balance framework for quantifying soil quality changes in response to soil formation-erosion imbalances at a river catchment scale. The utility of Ba isotope ratios for the practical application of this mass balance framework is demonstrated using data from the Irrawaddy and Salween river catchments, which span perturbations in erosional outputs due to seasonal hydroclimate variations and dam construction. In detail, this approach uses isotopic imbalances between Ba released by chemical weathering reactions and riverine export fluxes to quantify changes in soil exchangeable cation budgets. This new approach offers two capabilities for improved quantification of land degradation rates; (1) integration of soil formation-erosion imbalances over the same spatiotemporal scales with (2) direct constraints on the resulting changes in a key soil quality metric; cation exchange capacity (CEC).

2. Critical zone stable isotope mass balance theory

101

102 *2.1 An isotope mass balance framework for constraining soil formation-erosion*
103 *imbalances*

104

105 Soil formation involves a complexity of biogeochemical processes
106 transforming (primary) parent rock material into secondary phases. These secondary
107 phases include phyllosilicates and Fe-Al oxyhydroxides produced via chemical
108 weathering reactions, and organic matter and its degradation products produced by
109 biological processes. The composition and abundance of these secondary phases
110 underpin key soil functions. For example, secondary phases provide textural
111 properties that control soil water storage and aeration, serve as reservoirs for plant -
112 available nutrients and determine soil pH buffering capacity (Sposito et al., 1999,
113 Jobbágy and Jackson, 2001, Bullen and Chadwick, 2016, Ćirić et al., 2023). Soil
114 inventories of these secondary phases are controlled by the balances between soil
115 formation and soil erosion rates (Fig. 1). Changes in the abundance of these
116 secondary phases in response to perturbations to soil erosion vs formation rates, in
117 turn, drive declines in soil quality that underpins any associated land degradation.
118 Geochemical mass balance can potentially be used to track the growth and
119 depletion of critical zone secondary phase inventories (Fig. 1, Table 1). The storage of
120 elements within the critical zone secondary phases (sp) can be divided into 3 main
121 components; (1) elements stored within neo-formed secondary mineral crystal lattices
122 (sm), (2) elements structurally bound within organic matter, including both living and
123 dead biomass (org), and (3) elements adsorbed to the surfaces of secondary minerals
124 and organic matter, termed the exchange pool (ex). The rate at which this combined
125 elemental storage reservoir changes over time (F_{acc}) is a function of imbalances

between their elemental input (F_{in}) and output (F_{out}) fluxes (all in units of moles/time) (eqn. 1).

$$F_{acc} = F_{in} - F_{out} \quad \text{(eqn. 1)}$$

For elements that do not form gaseous species at Earth's surface conditions, inputs (F_{in}) are dominated by release from parent rock material via chemical weathering (F_{cw}) reactions, with additional contributions from wet and dry deposition of atmospheric aerosols (F_{atm}) (eqn. 2).

$$F_{in} = F_{cw} + F_{atm} \quad \text{(eqn. 2)}$$

Their outputs (F_{out}) are via a combination of solute leaching (F_{diss}) and erosion (F_{er}) (eqn. 3).

$$F_{out} = F_{diss} + F_{er} \quad \text{(eqn. 3)}$$

The application of Eqn. 1 to constrain imbalances in elemental budgets of critical zone secondary phases would require independent constraints on both F_{in} and F_{out}, integrated over similar spatiotemporal scales. Assuming wind erosion is negligible in a study area, F_{out} can be constrained from measurements of riverine dissolved (F_{diss}) and secondary phases in suspended particulate material (SPM) (F_{er}) loads (Fig. 1, Table 1). Independently constraining F_{in} is more challenging, as this is typically achieved using measurements of riverine chemical fluxes (F_{out}) (e.g. Gaillardet et al., 1999), with the assumption that critical zone elemental storage is at

steady state (i.e. $F_{acc} = 0$, so that $F_{in} = F_{out}$). Independent constraints on F_{in} can be obtained using soil production rates from cosmogenic nuclides (e.g. ^{10}Be) coupled with measurements of the chemical depletion of the chosen element between the soil and parent rock (e.g. von Blanckenburg et al. 2021). However, the resulting constraints on F_{in} and F_{out} in this case are integrated over vastly different temporal (instantaneous to multi-millennial) and spatial scales (single point to an entire river catchment), creating uncertainty in their comparison to reliably constrain F_{acc}.

Incorporating constraints from stable isotope compositions into critical zone elemental mass balance (eqn. 4) offers the potential to overcome challenges of obtaining simultaneous constraints on F_{in} and F_{out}.

$$\delta^{xx}X_{sp}\, F_{acc} = \delta^{xx}X_{in}\, F_{in} - \delta^{xx}X_{out}\, F_{out} \quad \text{(eqn. 4)}$$

Where $\delta^{xx}X$ represents the stable isotope composition (in delta notation) of element (X) in the input (in), output (out) and secondary phase (sp) accumulation fluxes of the critical zone storage reservoir (Fig. 1, Table 1). The output flux isotope composition ($\delta^{xx}X_{out}$) can be further decomposed into leaching (diss) and erosional components (eqn. 5).

$$\delta^{xx}X_{out} = \delta^{xx}X_{diss}\, f_{diss} + \delta^{xx}X_{sp}\, f_{er} \quad \text{(eqn. 5)}$$

Where f_{diss} and f_{er} is the fraction of the total output flux (F_{out}) composed by F_{diss} and F_{er} respectively (e.g. $f_{diss} = F_{diss}/ F_{out}$, with $f_{diss} + f_{er} = 1$). Isotopic composition differences between the different reservoirs/fluxes arise through isotope fractionations

175 accompanying the partitioning of element X between dissolved (diss) and secondary
176 phase (sp) reservoirs (eqn. 6).
177
178 $\Delta_{diss\text{-}sp} = \delta^{xx}X_{diss} - \delta^{xx}X_{sp}$ (eqn. 6)
179
180 Through substitution of eqn. 1, and rearrangement, eqn. 3 can be expressed in
181 the following form (eqn. 7) (Supplementary Information):
182
183 $$F_{acc} = F_{out}\left(\frac{\delta^{xx}X_{out} - \delta^{xx}X_{in}}{\delta^{xx}X_{in} - \delta^{xx}X_{sp}}\right)$$ (eqn. 7)
184
185 Here the accumulation/depletion rate of an element stored within secondary phases in
186 the critical zone (F_{acc}) can be determined by measuring the element's output flux
187 (F_{out}), scaled according to isotopic differences between the input flux ($\delta^{xx}X_{in}$), the
188 output flux ($\delta^{xx}X_{out}$) and the reservoir of element X accumulating in critical zone
189 secondary phases ($\delta^{xx}X_{sp}$). Note that this equation does not feature F_{in}. In theory, this
190 mass balance framework can therefore provide constraints on F_{acc} without issues of
191 variable spatiotemporal scales of integration that impact the currently available
192 approaches. If F_{acc} of element X can be further quantitatively linked to a soil quality
193 metric, then this framework could provide a quantitative assessment of associated
194 land degradation.
195
196 *2.2 Limits and assumptions of the isotope mass balance framework*
197
198 Isotopic variations between $\delta^{xx}X_{in}$, $\delta^{xx}X_{out}$ and $\delta^{xx}X_{sp}$, are controlled by the
199 relative partitioning of element X between leached and erosional fluxes (e.g. f_{diss}) and

the magnitude of the isotope fractionation between dissolved (diss) and secondary phase (sp) reservoirs ($\Delta_{diss\text{-}sp}$). Differences between $\delta^{xx}X_{in}$ and $\delta^{xx}X_{sp}$ (the denominator in eqn. 7) depend on $\Delta_{diss\text{-}sp}$ and the partitioning of element X between leaching (F_{diss}) and erosional (F_{er}) outputs at steady state ($f_{diss\text{-}ss}$; denotes f_{diss} under the condition that $F_{acc} = 0$) (eqn. 8; see Supplementary Information for derivation).

$$\delta^{xx}X_{in} - \delta^{xx}X_{sp} = f_{diss\text{-}ss}\,\Delta_{diss\text{-}sp} \quad \text{(eqn. 8)}$$

Differences between $\delta^{xx}X_{out}$ and $\delta^{xx}X_{in}$ (the numerator in eqn. 7) arise due to imbalances between F_{in} and F_{out} ($F_{acc} \neq 0$), which can likewise be re-expressed in terms of f_{diss}, $f_{diss\text{-}ss}$ and $\Delta_{diss\text{-}sp}$ (eqn. 9; see Supplementary Information for derivation).

$$\delta^{xx}X_{out} - \delta^{xx}X_{in} = \Delta_{diss\text{-}sp}\,(f_{diss} - f_{diss\text{-}ss}) \quad \text{(eqn. 9)}$$

Substitution of eqn. 8 and 9 into eqn. 7 and simplification leads to eqn. 10.

$$\frac{F_{acc}}{F_{out}} = \left(\frac{\delta^{xx}X_{out} - \delta^{xx}X_{in}}{\delta^{xx}X_{in} - \delta^{xx}X_{sp}}\right) = \left(\frac{f_{diss} - f_{diss-ss}}{f_{diss-ss}}\right) \quad \text{(eqn. 10)}$$

This shows that the ratio of the unknown F_{acc} to the measurable F_{out}, as quantified by differences between $\delta^{xx}X_{out}$, $\delta^{xx}X_{in}$ and $\delta^{xx}X_{sp}$, are equivalent to differences between the partitioning of leaching and erosional outputs of element X at a given moment (f_{diss}) relative to that at steady state ($f_{diss\text{-}ss}$) (Fig. 2).

Previous studies using isotope mass balance frameworks to constrain critical zone elemental cycling typically assume steady state conditions ($F_{acc} = 0$) to solve for the isotope fractionation factor ($\Delta_{diss\text{-}sp}$) and/or steady state partitioning between

dissolved and erosional outputs ($f_{diss\text{-}ss}$; the x-axis in Fig. 2) (e.g. Bouchez et al., 2013). For example, such steady state mass balance frameworks have been widely applied to Li isotope compositions to determine chemical vs physical denudation rates which are linked to $f_{diss\text{-}ss}$ of this element (Bouchez et al., 2013, Dellinger et al., 2015). Some studies have considered deviations from steady state for critical zone elemental storage based on stable isotope ratios, but without differentiation of primary vs secondary phase reservoirs within the mass balance framework (Charbonnier et al., 2022a). The key advancement of the mass balance framework proposed here is the consideration of deviations from steady state with respect to critical zone secondary phase storage (f_{diss} - $f_{diss\text{-}ss}$; the y-axis in Fig. 2).

The theoretical limits on F_{acc}/F_{out} are between -1 and infinity. The lower limit (-1) corresponds to the endmember situation where $F_{in} = 0$, so that $F_{acc} = -F_{out}$ (eqn. 1). The upper limit reflects that F_{in} could in theory be any positive value tending towards infinity. The isotope mass balance framework detailed above (eqn. 7 and 10) however, is constrained by further limitations on its ability of quantify F_{acc}/F_{out} within this theoretical range (Fig. 2). These limits vary as a function of $f_{diss\text{-}ss}$, the steady state ($F_{acc} = 0$) balance between leaching and erosional outputs of element X. At $f_{diss\text{-}ss}$ approaching 1 (i.e. close to 100% of element X exported by leaching at steady state with negligible erosion outputs), the isotope mass balance framework has good sensitivity for quantifying F_{acc}/F_{out} between 0 (steady state) and -1 (depletion of critical zone secondary phase stores) but has no sensitivity for quantifying positive F_{acc}/F_{out} (accumulation of critical zone secondary phase stores). Conversely, at $f_{diss\text{-}ss}$ approaching 0 (i.e. close to 100% of element X exported by erosion at steady state with negligible leaching outputs), the isotope mass balance framework has good

sensitivity for quantifying positive F_{acc}/F_{out} but no sensitivity for quantifying negative F_{acc}/F_{out}.

A key assumption underlying this mass balance framework is that the critical zone secondary phase storage reservoir behaves as a zero-dimensional 'batch reactor' for exchanging element X with the dissolved pool with an associated isotope fractionation (Bouchez et al., 2013). This assumes that there is no spatial variance in $\delta^{xx}X_{sp}$ within the critical zone storage reservoir and erosional outputs. A multitude of processes internally cycle elements between Critical Zone compartments (e.g. above ground biomass, soil horizons, saprolite) which can create spatial variance in $\delta^{xx}X_{sp}$ (Bullen and Chadwick, 2016, Gong et al., 2020). This can impact the application of this mass balance framework because the $\delta^{xx}X_{sp}$ of riverine erosional outputs (F_{er}) could differ from that of the weighted average of the critical zone storage reservoir (F_{acc}). Spatial segregation of secondary phases along fluid flow pathways within the critical zone can also be associated with Rayleigh distillation effects on the isotope composition of dissolved exports (e.g., $\delta^{xx}X_{diss}$, Tipper et al., 2012, Bouchez et al., 2013, Dellinger et al., 2015), in turn decoupling the relationship between $\delta^{xx}X_{diss}$ and $\delta^{xx}X_{sp}$ in river exports ($\Delta_{diss\text{-}sp}$; eqn. 6), as well as the relationships between $\delta^{xx}X_{sp}$, $\delta^{xx}X_{out}$ and $\delta^{xx}X_{in}$ assumed by the model (eqn. 7 and 10). The extent to which Rayleigh distillation effects can arise within the critical zone depends on the rate of reversible exchange of element X between the dissolved and secondary phases reservoirs compared to the transit times of dissolved and solid material fluxes through the critical zone. As the forward and backward reaction rates of element X between the dissolved pool and the secondary phases approach a balance, the associated changes in isotopic composition should approximate batch rather than Rayleigh type model behavior (Bouchez et al., 2013).

Gaining constraints on soil formation-erosion imbalances using the mass balance framework requires further assumptions. Specifically, that the calculated F_{acc} relates to changes in the soil associated secondary phase reservoir driven by perturbations to erosional outputs. However, the mass balance framework more strictly considers the entire critical zone secondary phase storage reservoir, including F_{acc} components associated with changes in above ground biomass and deeper, erosion-unaffected saprolite. Furthermore, perturbations to leached outputs could in theory drive changes in F_{acc}, for example via soil pH changes which can impact the exchangeable base cation reservoir. Interpreting F_{acc} constraints in terms of soil formation-erosion balances versus these other possible drivers therefore requires wider contextual considerations of the isotope system and study area in question.

2.3 Requirements for the practical application of the mass balance framework

The practical application of the mass balance framework described in section 2.1 requires a stable isotope system that has; (1) sufficient sensitivity in elemental partitioning (f_{diss}) between dissolved and secondary phases and an associated isotope fractionation ($\Delta_{diss\text{-}sp}$), (2) the ability to reliably constrain F_{out}, $\delta^{xx}X_{sp}$, $\delta^{xx}X_{out}$ and $\delta^{xx}X_{in}$ from field measurements, (3) attributes to its internal critical zone cycling that allow approximation to zero-dimensional 'batch reactor' type behavior and (4) a quantitative link between F_{acc} of element X to a soil quality metric that can be used to quantify associated land degradation.

The sensitivity of eqn. 7 for constraining F_{acc} depends on the magnitude of $\Delta_{diss\text{-}sp}$ compared to measurement uncertainty for $\delta^{xx}X_{sp}$, $\delta^{xx}X_{out}$ and $\delta^{xx}X_{in}$ (Fig. 2). It also depends on differences between f_{diss} and $f_{diss\text{-}ss}$ being sufficiently sensitive to

299 erosional perturbations of interest. There are a number of previously developed stable
300 isotope systems which could fit these requirements, notably those of the alkali and
301 alkaline earth elements (e.g., Li, K, Ca, Mg, Sr, Tipper et al., 2012, Bouchez et al.,
302 2013, Dellinger et al., 2015). The elemental partitioning and associated isotope
303 fractionations of these systems are dominated by uptake into secondary mineral lattice
304 (sm) and organic matter (org) components of the secondary phase reservoir (Fig. 1).
305 The nature of this phase partitioning, however, creates challenges for meeting
306 requirements (2) and (3) raised in the paragraph above.

307 Constraining F_{out}, $\delta^{xx}X_{out}$ and $\delta^{xx}X_{sp}$ using river SPM samples requires that
308 neo-formed secondary phases containing element X are isolated from primary phases.
309 Sequential leaching techniques can be applied to this end but are limited in their
310 reliability in quantitatively isolating certain secondary mineral (sm) and organic
311 matter (org) hosted element pools. Elements hosted in secondary phyllosilicates, for
312 example, exhibit similar solubilities to those hosted in primary silicate minerals.
313 Furthermore, a significant component of elements hosted in phyllosilicates and
314 organic matter in river SPM loads may in fact originate from the parent rock material
315 (i.e. are primary minerals), rather than neo-formed secondary phases produced by
316 contemporary critical zone processes (e.g., Dellinger et al., 2014). These
317 complications inhibit the ability to reliably constrain all the terms in eqn. 7 to solve
318 for imbalances in critical zone elemental storage. Reflecting this uncertainty,
319 previously developed isotope mass balance applications tend to assume steady state
320 conditions ($F_{acc} = 0$) to be able to then solve for these hard-to-constrain terms (e.g.
321 Bouchez et al., 2013). Furthermore, the slow kinetics of elemental uptake/release
322 from these phases, relative to fluid transit times in the critical zone, make the

323 associated isotope effects prone to Rayleigh-type behavior (e.g. Dellinger et al.,
324 2015).
325
326 *2.4 The utility of Ba isotopes for application to the mass balance framework*
327
328 Partitioning of elements between dissolved and exchange pools (ex) with an
329 associated isotope fractionation offers advantages over those of secondary mineral
330 lattice (sm) and organic matter (org) pools for meeting the criteria for applying the
331 mass balance framework described in section 2.1. Firstly, established leaching
332 protocols exist for the reliable separation of the exchange pool from primary phases in
333 river SPM samples (Tessier et al., 1979, Tipper et al., 2021, Knight et al., 2024a).
334 Secondly, chemical equilibrium between the dissolved and exchange pool is achieved
335 on short timescales (~seconds to days; Tang and Sparks, 1993, Knight et al., 2024b)
336 relative to critical zone fluid residence times (typically weeks to years, Jasechko et al.,
337 2016), which should mitigate against potential Rayleigh-type isotope effects. We
338 therefore propose that an element which partitions predominantly between dissolved
339 and exchange pools within the critical zone with an associated isotope fractionation
340 should be best suited for the application of this mass balance framework.
341 Constraining F_{acc} related to an element's storage within the critical zone
342 exchange pool reservoir offers the potential to provide quantitative constraints on
343 changes in soil cation exchange capacity (CEC) in response to erosional perturbations.
344 Soil CEC is a key soil quality metric that determines soil plant available nutrient
345 stores and pH buffering capacity (Ćirić et al., 2023). It is controlled by the abundance
346 and composition of secondary minerals and organic matter, and therefore tends to
347 correlate with other soil quality parameters linked to these phases (Drescher et al.,

2024). Quantifying changes in soil CEC in response to perturbations to soil erosion-formation balances would therefore provide a key quantitative metric for associated land degradation.

For most alkali/alkaline earth elements (Na, K, Li, Ca, Mg, Sr) exports via the exchange pools of river SPM loads typically represent <<10% relative to dissolved load fluxes (Tipper et al., 2021, Knight et al., 2024a), so have limited leverage on f_{diss} (eqn. 10). The alkaline earth metal Ba however, preferentially partitions into the exchange pool relative to other major alkali/alkaline earth group elements (Na, K, Li, Ca, Mg, Sr, Teppen and Miller, 2006). Reflecting this, exchangeable Ba on SPM loads constitutes a significant fraction of riverine export fluxes (~25 to 75% relative to dissolved fluxes), with variability in this partitioning linked to the magnitude of erosional fluxes (Bridgestock et al., 2021, Knight et al., 2024b).

Recent studies have explored the use of Ba isotope ratios for tracing critical zone processes (Bullen and Chadwick, 2016, Gou et al., 2020, Gong et al., 2020, Charbonnier et al., 2020, Charbonnier et al., 2022a, Charbonnier et al., 2022b, Knight et al., 2024b). These past studies have revealed that river dissolved loads are enriched in heavier Ba isotopes relative to average rocks, which are normally taken to represent the composition of chemical weathering inputs (Gou et al., 2020, Charbonnier et al., 2020, Charbonnier et al., 2022a, Charbonnier et al., 2022b). Experimental and field constraints suggest that the magnitude of this offset can be feasibly explained by a Ba isotope fractionation accompanying dissolved-exchange pool partitioning (Bridgestock et al., 2021, Cao et al., 2021, Knight et al., 2024b). Furthermore, the exchangeable Ba content of uplifted marine sediments should be negligible, mitigating against issues of discriminating between neo-formed and parent material derived elemental budgets (Knight et al, 2024b). Overall, these characteristics suggest

373 Ba isotope ratios could be well suited for application to mass balance framework
374 described in section 2.1. However, questions remain over the potential importance of
375 Ba incorporation into secondary mineral lattice (sm) and organic matter pools (org)
376 during critical zone processes (Bullen and Chadwick, 2016, Charbonnier et al., 2020,
377 Charbonnier et al., 2022b).
378 In the following, data for co-located river water and SPM samples collected in
379 the Irrawaddy and Salween catchments are used to; (1) provide quantitative
380 constraints on the relative partitioning of Ba between dissolved (diss), exchangeable
381 (ex), secondary mineral (sm) and organic (org) reservoirs in river outputs, (2) assess
382 the consistency of Ba isotope behavior relative to the proposed mass balance
383 framework, and (3) demonstrate the utility of this isotope system to quantify changes
384 in soil exchangeable cation budgets in response to erosional perturbations in these
385 catchments.
386
387 **3. Study area and samples**
388
389 *3.1 Characteristics of the Irrawaddy and Salween River catchments*
390
391 The Irrawaddy (436,500 km^2) and Salween (282,300 km^2) are two of the
392 major river catchments draining the Himalayan Mountain range and it's foothills (Fig.
393 3, Chapman et al., 2015, Baronas et al., 2020, Latrubesse et al., 2021). They are
394 among the last remaining large river catchments that feature only limited modification
395 to their hydrological networks (Grill et al., 2019) and have large areas that are only
396 minimally impacted by land use changes (Salmivaara et al., 2013, Bhagwat et al.,
397 2017). Key exceptions include three major Irrawaddy River tributaries (Mu, Myitnge

398 and Shweu) which have been dammed (Chen et al., 2020). Mining activities are also
399 proposed to have increased riverine sediment transport in the Irrawaddy River
400 catchment relative to the natural baseline (Dong et al., 2025). The hydrology of these
401 catchments is controlled by seasonal climate variations, driven by the southwest Asian
402 monsoon, with discharge increasing by ~10 fold between the dry (October to April)
403 and monsoon seasons (May to September) (Furuichi et al., 2009) (Fig. 3bc). The
404 Irrawaddy River catchment features extensive floodplains in the central basin and
405 delta regions of the catchment which experience flooding during the monsoon season.
406 By contrast, the Salween River catchment features almost no floodplain area.
407 The annual SPM (325 and 159 Mt/yr) and dissolved (52 and 45 Mt/yr) loads
408 of the Irrawaddy and Salween rivers rank in the top 10 globally (Milliman and
409 Farnsworth, 2011, Chapman et al., 2015, Baronas et al., 2020). These estimates
410 suggest that these catchments are dominated by physical denudation (erosion-SPM
411 exports) (~70 to 85%), with chemical denudation (leaching-dissolved exports)
412 accounting for ~15 to 30%. These fluxes exhibit large seasonal variations linked to
413 monsoonal climate variability. Fluxes of SPM increase by a factor of ~60 between the
414 dry (October to April) and monsoon seasons (May to September) (Baronas et al.,
415 2020), whereas dissolved solute fluxes, including Ba, increase by only a factor of ~ 4
416 to 10 (Chapman et al., 2015, Bridgestock et al., 2022) (Fig. 3bc).
417 The characteristics described above lead to three testable hypotheses regarding
418 the Ba isotope ratio dynamics of these river catchments in context of the proposed
419 mass balance framework (Fig. 2, eqn. 10). Firstly, since total denudation is dominated
420 by physical denudation (erosion) in these catchments, $f_{diss\text{-}ss}$ is hypothesized to be
421 close to 0 so that $\delta^{138/138}Ba_{sp}$ tends towards $\delta^{138/134}Ba_{in}$ (eqn. 8). Secondly, seasonal
422 changes in SPM versus dissolved exports should cause systematic changes in f_{diss},

corresponding to variations in $\delta^{138/134}Ba_{out}$ - $\delta^{138/134}Ba_{in}$ (eqn. 9) and hence F_{acc} (eqn. 10). Thirdly, dam construction in the river Mu, Myitnge and Shweu sub-catchments is likely to have reduced their SPM fluxes, increasing f_{diss} relative to $f_{diss\text{-}ss}$, again corresponding to variations $\delta^{138/134}Ba_{out}$ - $\delta^{138/134}Ba_{in}$ (eqn. 9) and hence F_{acc} (eqn. 10).

3.2 Sample collection locations and times

Co-located filtered river water (< 0.22 μm), SPM (> 0.22 μm) and bank sand samples were collected at nine locations in the Irrawaddy River catchment and one location in the Salween River catchment during 3 different time periods (February 2018, August 2018 and May 2019) (Fig 3a). These sampling time periods capture the full range of the annual hydrograph, including low (3000 m^3/sec at Pyay, February 2018), rising (5300 m^3/sec at Pyay, May 2019) and peak (32100 m^3/sec at Pyay, August 2018) discharge conditions (Fig. 3bc) (Baronas et al., 2020). Sampling locations include 4 sites spanning the length of Irrawaddy main stem: from Myitkyina, ~50 km downstream from the headwater tributaries, to Pyay, ~100 km upstream from bifurcation of its delta distributaries. Five sampling locations are on Irrawaddy tributaries, including the headwaters (the Mali Kha and Nmai Kha), the 3 dammed sub-catchments (the Mu, Myitnge and Shweu) and the Chindwin River, the largest Irrawaddy tributary which supplies ~50% of the Irrawaddy River catchment's total discharge and the SPM load (Chapman et al., 2015, Garzanti et al., 2016). During the August 2018 and May 2019 sampling campaigns, depth profiles of river SPM samples were collected at Irrawaddy River main stem (at Pyay, Bagan and Mandalay), Chindwin River and the Salween River sites. During February 2018, and at other locations, only surface SPM samples were collected. In addition, five rain

samples were collected (1 in August 2017, 3 in August 2018 and 1 in May 2019) to assess endmember compositions for atmospheric inputs. Finally, three reference clay samples obtained from the Clay Mineral Society, KGa-2 (kaolinite), SWy-2 (montmorillonite) and ISCz-1 (illite-smectite 70/30 mixture) were analyzed to assess the importance of Ba partitioning into secondary mineral lattice sites (Vogt et al., 2002). These clay types represent the 3 most abundant secondary phyllosilicate phases occurring within the critical zone (Ito and Wagai, 2017).

4. Analytical methods

4.1 Sampling protocols

River water samples were collected using a custom built Van Dorn-style sampler as described by Baronas et al. (2020). Following collection, samples were filtered (0.22 μm, polyethersulfone membrane), with water collected into acid cleaned high-density polyethylene (HDPE) bottles and acidified to pH <2 using distilled 16 M HNO_3. Separate un-acidified filtered water samples were also collected for dissolved anion measurements into amber HDPE bottles that were pre-cleaned by rinsing with milli-Q water. Water pH and temperature were measured in the field using a Hanna instruments HI 991300 meter equipped with a HI-1288 electrode. Suspended particulate material samples were washed off the filters into opaque glass jars using un-acidified filtered water from the same sample and were subsequently freeze-dried. Bank sand samples were collected from recent riverbank deposits (containing no plant matter) and were subsequently freeze dried. River water discharge was determined using measurements of channel-wide flow velocity distributions using an Acoustic

Doppler Current Profiler (ADCP) as described by Baronas et al. (2020). Rainwater samples were collected either into acid-cleaned high-density polyethylene bottles or from plastic sheeting. Rainwater was filtered through a 0.22 μm polyethersulfone capsule filter (Millex-GP, 33 mm diameter) using a syringe with aliquots collected for cation (acidified) and anion analyses (un-acidified) as described for the river waters.

4.2 Measurement of dissolved solute concentrations

Concentrations of dissolved cations (Na, Ca, Mg, K, Sr, Ba) and silica were measured on acidified filtered water samples using inductively coupled plasma optical emission spectroscopy (ICP-OES; Agilent 5100) at the University of Cambridge in the Department of Earth Sciences (Larkin et al., 2021). Repeat analyses of certified reference materials SLRS-6 (National Research Council, Canada) and SPS-SW2 (Spectrapure Standards AS, Oslo, Norway) yielded reproducibility (2SD) of < 5% for most elements and were within uncertainty of certified values (Supplementary Table 1). Concentrations of dissolved anions (Cl^- and SO_4^{2-}) were determined on un-acidified samples by ion chromatography (Thermo Scientific Dionex ICS-5000+ High Performance-4 Ion Chromatograph) with typical reproducibility of ~2%.

4.3 Measurement of riverine sediment elemental compositions

Freeze-dried SPM samples were weighed to determine SPM concentrations. The particle size distributions and organic carbon concentrations of select SPM and bank sand samples were determined as described by Baronas et al. (2020). Dried SPM and bank sand samples were gently disaggregated using an agate pestle and mortar.

Aliquots of ~0.4 g of sediment were then subjected to a sequential leaching procedure to partition elements associated with different phases; (1) the exchange pool (1 M NH_4Cl), (2) metal (oxyhydr)oxides ('HH'; 5 mM hydroxylamine hydrochloride+ 3 M Na-EDTA+1.5% acetic acid buffered to a pH of ~4 with NaOH), (3) calcite and other carbonates (1.7 M acetic acid), (4) dolomite and remaining crystalline metal (oxyhydr)oxides (1 M HCl) and (5) silicates (loss on ignition followed by total digestion by lithium borate fusion) (Supplementary Table 2). Elemental concentrations of these leachates were determined using ICP-OES, with matrix matched calibration curves as described in detail by Larkin et al. (2021). Blanks associated with these steps correspond to <3.8% of the extracted Ba.

Radiogenic Sr isotopes were determined for filtered river water samples and paired 1 M NH_4Cl leachates (step 1; exchange pool) to monitor for any unwanted mineral dissolution at this leaching step (Supplementary Information). These radiogenic Sr isotope compositions were determined using multiple collector inductively coupled plasma mass spectrometry using protocols described by Stevenson et al. (2025). To assess how quantitatively Ba (and other cations) are extracted from the exchange pool using the single 1 M NH_4Cl step employed in this study, three suspended sediment samples (IRR18-229, IRR18-230 and IRR18-184) were also subjected to a modified version of the sequential leaching procedure, consisting of three repeat 1 M NH_4Cl leaches, followed by the HH step (Supplementary Information).

4.4. Reference clay samples

The Clay Mineral Society's reference clays, SWy-2 (montmorillonite) and ISCz-1 (illlite-smectite mixture) are known to contain 13.3% and 10.1% of impurities, respectively, notably quartz (5.2% and 0.7%), plagioclase (0.1% and 5.5%), K-feldspar (0% and 2.3%) and clinopyroxene (4.4% and 0%) (Vogt et al., 2002). The clay fraction of these materials were subject to further purification by suspension within milli-Q water and centrifugation at 125 G for 10 mins as described by Knight et al. (2024b). The supernatant containing the suspended clay fraction was isolated from the coarser impurities, with the process repeated three times. The reference clay KGa-2 by contrast only contains 1.2% impurities (Vogt et al., 2002), so that no further purification by centrifugation was deemed necessary. Aliquots of the clay minerals (~0.15 g) were then accurately weighed and subjected to steps 1 (1 M NH_4Cl), 2 (5mM HH) and 3 (1.7 M acetic acid) of the sequential leaching procedure described in section 4.3 to remove elements associated with the exchange pool, metal oxyhydroxides and carbonates, respectively. The residues were then subjected to total digestion in 0.7ml 16 M HNO_3 + 0.7 ml 28 M HF at 120˚C, dried down, followed by 1.66 ml 10 M HCl + 0.44 ml 16 M HNO_3 at 120˚C, and dried down again, prior to dissolution in 0.3 M HNO_3. Elemental concentrations (Ba, Al, Ca, Fe, K, Li, Mg, Mn, Na, P, Sr and Ti) of these digested solutions were then determined by ICP-OES with a matrix matched calibration line.

4.4 Measurement of barium isotope compositions

Barium isotope compositions were determined for 83 samples, including 16 filtered river waters, 18 NH_4Cl sediment leachates, 13 HH sediment leachates, 3 acetic acid sediment leachates, 18 sediment residues, 3 reference clay samples and 12

leachate test samples. Barium isotope compositions were measured using thermal ionization mass spectrometry (TIMS; Triton Plus, Thermo Scientific at the University of Cambridge), with instrumental mass bias corrected using a ^{130}Ba-^{135}Ba double spike solution, as described by Knight et al. (2024b). In brief, sample aliquots containing 200 ng of Ba were equilibrated with a known quantity of the Ba double spike solution to achieve a molar spike/sample ration of 0.2. These sample-double spike mixtures were processed through a cation exchange chromatography procedure to purify Ba from sample matrices, prior to isotopic analyses by TIMS. The procedural blank (chromatography + TIMS measurement) ranged between 0.01 and 0.67 ng (n = 7) representing <0.33 % of the Ba processed in the samples. Barium isotope compositions are expressed as $\delta^{138/134}$Ba values (eqn. 11) relative to the standard reference material (SRM) NIST 3104a:

$$\delta^{138/134}Ba\ ‰ = \left(\frac{^{138}Ba/^{134}Ba_{sample}}{^{138}Ba/^{134}Ba_{NIST3104a}} - 1\right) \times 1000 \qquad \text{(eqn. 11)}$$

Barium concentrations were determined from the isotopic analyses by isotope dilution.

The long-term reproducibility of the $\delta^{138/134}$Ba values was ± 0.04 ‰ (2SD) based on repeat measurements of SRM NBS-127 over the course of the study (n = 31). This level of reproducibility was taken to represent the uncertainty of the samples. Exceptions to this are 7 sample analyses that exhibited internal errors (2SE of replicate integrations of an individual analysis) higher than ± 0.04 ‰ due to low ion beam intensity. For these analyses, uncertainty is taken as the internal error. Accuracy was validated by measurement of SRM NBS-127 and the geological SRMs BCR-2, BHVO-2, AGV-2 and JB-2, with results agreeing within uncertainty of those

572 reported by other laboratories (Miyazaki et al., 2014, Nan et al., 2015, van Zuilen et
573 al., 2016, Horner et al., 2017, Nan et al., 2018, Tian et al., 2019, Geymann et al.,
574 2019, An et al., 2020, Tieman et al, 2020, Bridgestock et al., 2021) (Supplementary
575 Fig. 6). Barium concentrations determined by isotope dilution from the TIMS
576 analyses agree within 10% of those determined by ICP-OES (Supplementary Fig. 7).
577
578 *4.5 Calculation of derived parameters*
579
580 The combined Ba budgets of steps 1 (1 M NH_4Cl) and 2 (5 mM HH) of the
581 sequential leaching procedure are taken to represent that of the neo-formed secondary
582 phase Ba budget ($[Ba]_{sp}$ and $\delta^{138/134}Ba_{sp}$; Supplementary Information). This is based
583 on results of tests to the sequential leaching procedure (section 5, Supplementary
584 Information), and the observation that elements within the 5 mM HH leaching step are
585 able to rapidly equilibrate with the dissolved pool in rivers (Larkin et al., 2021) The
586 total riverine export flux of dissolved (diss) and secondary phase (sp) Ba, (F_{out}) is
587 calculated by eqn 12, with the fraction of this flux occurring via leaching (f_{diss})
588 calculated by eqn. 13.
589
590 $$F_{out} = Q\left([Ba]_{diss} + SPM[Ba]_{sp}\right) \quad \text{(eqn. 12)}$$
591
592 $$f_{diss} = \frac{[Ba]_{diss}}{[Ba]_{diss}+SPM[Ba]_{sp}} \quad \text{(eqn. 13)}$$
593
594 Where Q denotes the river discharge (L/time), $[Ba]_{diss}$ is the Ba concentration of the
595 filtered river water (µmol/L), $[Ba]_{sp}$ is the Ba concentration of the SPM associated
596 with neo-formed secondary phases (µmol/g) and the other terms are as specified in

section 2. The Ba isotope composition of F_{out} ($\delta^{138/134}Ba_{out}$) is calculated using eqn. 5, where '$\delta^{xx}X$' now denotes $\delta^{138/134}Ba$.

The CEC of the river sediment samples are calculated using as the sum of the charge of the major cations (Na, K, Ca and Mg) liberated by leaching step 1 and $[Ba]_{sp}$ in units of μmol/g (eqn. 14):

$$CEC\ \left(\frac{meq}{100g}\right) = \frac{2[Ca]+2[Mg]+2[Ba]_{sp}+[Na]+[K]}{10} \quad \text{(eqn. 14)}$$

The fraction of the CEC that supported by Ba is expressed as β_{Ba} (eqn. 15):

$$\beta_{Ba} = \frac{2[Ba]_{sp}}{CEC \times 10} \quad \text{(eqn. 15)}$$

5. Results

Data for river water, river sediment, rain and the reference clays presented in this study can be found in the Supplementary Data file. Barium within the riverine sediment samples is predominantly associated with the residue (median fraction of 86.4%) and 1 M NH_4Cl (median fraction of 7.6%) steps of the sequential leaching procedure (Fig. 4). The 5 mM HH, 1.7 M acetic acid, and 1 M HCl fractions host 1.7%, 0.5% and 3.3% (median fractions) of the total Ba in the sediments respectively. Results from the sequential leaching tests show that the single 1 M NH_4Cl step utilized in this study only liberates ~80% of NH_4Cl-extractable Ba in the river sediments (Supplementary Information). The remainder is liberated in the 5 mM HH step, constituting ~50% of the Ba measured in this fraction. River sediment $[Ba]_{sp}$ increases with CEC, following relationships corresponding to β_{Ba} values ranging

between 0.002 to 0.005 for most samples (Fig. 5). In turn, CEC is linked to grain size (D_{50}), decreasing towards coarser fractions.

The $\delta^{138/134}$Ba values of the river dissolved loads (0.25 ± 0.03 ‰; mean ± 2SE, n = 15) are systematically offset to higher values relative to those of the river sediment residue fractions (-0.03 ± 0.03 ‰; mean ± 2SE, n = 19) (Fig. 6). The latter are consistent with the isotope composition of average upper continental crust of $\delta^{138/134}$Ba = 0.00 ± 0.04 ‰ (Nan et al., 2018), while the former are consistent with literature data for other river dissolved loads (0.1 to 0.6 ‰; Gou et al., 2020, Cao et al., 2020, Charbonnier et al., 2020, Bridgestock et al., 2021, Charbonnier et al., 2022a, Charbonnier et al., 2022b, Knight et al., 2024b). River dissolved load $\delta^{138/134}$Ba values are also systematically offset to higher values relative to river sediment 1 M NH_4Cl (0.02 ± 0.02 ‰; mean ± 2SE, n = 18) and 5 mM HH (0.02 ± 0.03 ‰; mean ± 2SE, n = 13) extractions. The means of the $\delta^{138/134}$Ba values for the NH_4Cl and HH extractions are identical to each other and similar to, but slightly higher, than that of the residue fraction of the river sediment samples (-0.03± 0.03 ‰; mean ± 2SE, n = 19). The mean offset between the $\delta^{138/134}$Ba values of co-located river water-SPM hosted secondary phase Ba ($\Delta_{diss\text{-}sp}$ = 0.23 ± 0.14 ‰; mean ± 2SD, n = 18; eqn. 6) is consistent with other field observations and experimental results for Ba isotope fractionation accompanying adsorption onto phyllosilicates and Fe-oxyhydroxides (Knight et al., 2024b).

The $\delta^{138/134}$Ba values of the sediment residues decrease with increasing grain size (D_{50}) and Si/Al ratios (a proxy for river sediment grain size; Bouchez et al., 2011) (Fig. 7). Sediment residue $\delta^{138/134}$Ba values are also positively correlated with residue Al/Ba (r^2 = 0.35), while residue Ba/Al are positively correlated with residue Si/Al (r^2 = 0.83). The clay reference samples (KGa-2, SWy-2 and ISCz-1) exhibit a higher

range of $\delta^{138/134}$Ba values relative to the sediment residues of 0.02 ‰ (KGa-2; kaolinite), 0.18 ‰ (Swy-2; montmorillionite) and 0.22 ‰ (ISCz-1; illite-smectite mixture). Clay reference samples also feature Al/Ba (Ba/Al) ratios 7 to 41 times higher (lower) than those of the river sediment residues, and plot off the linear relationships between river sediment residue $\delta^{138/134}$Ba, Al/Ba and Si/Al.

Variability in f_{diss} spans almost the full range of this parameter, from 0.05 to 0.94, decreasing as a function of SPM concentration, which varies between 0.03 and 6.9 g/L (Fig. 8a). The Salween River has a higher $[Ba]_{diss}$ (178 to 186 nmol/L) compared to those of the Chindwin and Irrawaddy rivers (30 to 84 nmol/L) causing a slight offset in the f_{diss} vs SPM relationships between these datasets. The lowest SPM concentrations, and consequently highest f_{diss}, correspond to the dammed tributaries sampled during the monsoon season (August 2018; rivers Mu, Myitnge, Shweu; SPM = 0.03 to 0.04 g/L, f_{diss} = 0.75 to 0.94) and samples of the Irrawaddy and Chindwin rivers collected during the dry season (February 2018; SPM = 0.06 to 0.13 g/L, f_{diss} = 0.69 to 0.79). The highest SPM concentrations, and hence lowest f_{diss}, correspond to the Chindwin (SPM = 1.2 to 4.2 g/L, f_{diss} = 0.05 to 0.09), Salween (SPM = 1.3 to 6.9 g/L, f_{diss} = 0.13 to 0.27) and the Irrawaddy at Pyay (SPM = 0.76 to 1.25 g/L, f_{diss} = 0.18 to 0.19) sampled during the monsoon season (August 2018). The $\delta^{138/134}Ba_{diss}$ and $\delta^{138/134}Ba_{sp}$ display no systematic relationship to f_{diss} or SPM concentrations (Fig. 8b). The $\delta^{138/134}$Ba combined dissolved and exchangeable riverine outputs ($\delta^{138/134}Ba_{out}$) (eqn. 5), consequently increases systematically from 0 to 0.2 ‰ with decreasing SPM (hence increasing f_{diss}). As discussed below, these systematic changes of the $\delta^{138/134}$Ba of riverine outputs SPM and f_{diss} are consistent with the mass balance framework described in section 2.

672

673 **6. Discussion**

674

675 In the following, field data are used to constrain the terms of the mass balance
676 framework (section 2.1, eqn. 7) and assess the utility of stable Ba isotope ratios to
677 constrain soil CEC changes in response to soil formation-erosion perturbations. First,
678 the constraints on $\delta^{138/134}Ba_{in}$ are discussed (section 6.1), prior to evaluating
679 assumptions regarding the calculation of F_{out}, $\delta^{138/134}Ba_{out}$ and $\delta^{138/134}Ba_{sp}$ (section
680 6.2). Next the variability in $\delta^{138/134}Ba_{out}$ - $\delta^{138/134}Ba_{in}$ are discussed in context of the
681 known erosional perturbations captured by the sample set to provide validation to the
682 mass balance framework (section 6.3). Finally, the mass balance framework is applied
683 to quantify imbalances in catchment wide soil exchangeable cation budgets in
684 response to seasonal climate perturbations, demonstrating the utility of this new
685 approach (section 6.4).

686

687 *6.1 Constraints on $\delta^{138/134}Ba_{in}$*

688

689 The supply of Ba to the critical zone secondary phase reservoir (F_{in}, eqn. 2)
690 should be dominated by chemical weathering reactions (cw), although some
691 contribution could also come from the deposition of atmospheric aerosols (atm) (Fig.
692 2). The relative proportions of these two input fluxes are estimated by comparing the
693 Ba concentrations of the rainwater samples ($[Ba]_{rain}$) to those of the combined
694 dissolved and SPM exchangeable pools in the river waters (eqn. 16).

695

696 $$f_{atm} = \frac{[Ba]_{rain}}{[Ba]_{diss} + SPM[Ba]_{sp}} \quad \text{(eqn. 16)}$$

Where f_{atm} is the fraction of F_{in} supplied by atmospheric inputs. Note that this relies on the simplifying assumptions that $F_{acc} = 0$, dry deposition supplies negligible atmospheric inputs and rainwater concentrations are not further impacted by evapotranspiration. Nonetheless, these estimates provide a useful first order assessment of relative importance of these two F_{in} components.

Rainwater Ba concentrations range between 2.4 and 27.7 nmol/L, consistent with literature data from other regions (Tripathy et al., 2019). Using the median $[Ba]_{rain}$ of 10.9 nmol/L, values of f_{atm} range between 0.01 and 0.16, with a mean of 0.07. The Ba in the rainwater likely derives from mineral dust dissolution, based on the positive correlation between rainwater Ba and Al concentrations (Supplementary Fig. 8). Therefore, although atmospheric deposition likely supplies ~1 to 10% of F_{in}, it is derived from similar source material and processes as the chemical weathering input (i.e. dissolution of mineral phases).

The mean $\delta^{138/134}Ba$ value of the river sediment residue fractions (-0.03 ± 0.03 ‰; mean ± 2SE, n = 19; Fig. 6) should represent the average isotope composition of parent material suppling both F_{cw} and F_{atm} components of F_{in}. Notably this composition is within uncertainty of estimates of the upper continental crust (0.00 ± 0.04 ‰; Nan et al., 2018) lending confidence to this assumption (Fig. 7). Assuming that there is no Ba isotope fractionation accompanying the dissolution of this parent material then this composition should represent $\delta^{138/134}Ba_{in}$.

There are two viable interpretations of the relationships between river sediment residue $\delta^{138/134}Ba$, grain size (Si/Al) and Al/Ba (Ba/Al) (Fig. 7), which have implications for using average residue $\delta^{138/134}Ba$ to constrain $\delta^{138/134}Ba_{in}$. Firstly, the relationships could reflect mixing between two distinct Ba hosting mineral

722 populations; one concentrated in the coarser sized fraction (high Si/Al) featuring low
723 $\delta^{138/134}$Ba and high Ba/Al, the other concentrated in the finer grain sized fraction (low
724 Si/Al) featuring high $\delta^{138/134}$Ba and low Ba/Al. Secondary phyllosilicates are ruled out
725 as the fine grain sized endmember, as the clay reference samples feature much lower
726 Ba/Al and $\delta^{138/134}$Ba than those predicted by the mixing lines. The major primary
727 silicate phases for hosting Ba are k-feldspar in addition to biotite and muscovite mica
728 (Deng et al., 2021). Mineral separate literature data shows that the micas could
729 feasibly account for the high $\delta^{138/134}$Ba - low Ba/Al endmember, while k-feldspar
730 could account for the low $\delta^{138/134}$Ba - low Ba/Al endmember (Fig. 7c) (Deng et al.,
731 2021). Note that while the Si/Al ratios of k-feldspar are lower than the endmember
732 required by the sediment residue data, this is likely explained by quartz dilution
733 elevating the Si/Al of the latter (Bouchez et al., 2011). The implications of this
734 interpretation are that micas and k-feldspar are physically separated by hydrodynamic
735 processes during river transport, which in turn impacts residue $\delta^{138/134}$Ba. Micas
736 (higher $\delta^{138/134}$Ba) are concentrated in the finer grain size fractions which are
737 preferentially transported by river SPM loads, resulting in a relative enrichment in k-
738 feldspar (lower $\delta^{138/134}$Ba) in the coarser bank sands. In turn this means that the
739 average residue $\delta^{138/134}$Ba could be biased from that of the average parent material,
740 depending on the weighing of the grain sizes of the sampled population, an issue that
741 is discussed further in section 6.3.

742 An alternative interpretation is that relationships between river sediment
743 $\delta^{138/134}$Ba and Al/Ba (Fig. 7) could arise due to the preferential release of the lighter
744 Ba isotopes during chemical weathering. This would drive a coupled increase in
745 residue $\delta^{138/134}$Ba and Al/Ba as observed. Gong et al. (2020) made similar
746 observations of increased residue $\delta^{138/134}$Ba as a function of Ba depletion in a laterite

747 weathering profile. Their study also conducted basalt dissolution experiments where
748 the released Ba featured $\delta^{138/134}$Ba 0.4 to 0.9 ‰ lower than the bulk rock. These
749 observations could be explained by preferential dissolution of mineral phases
750 featuring lower $\delta^{138/134}$Ba than the bulk rock and/or processes that induce an isotope
751 fractionation during chemical weathering. The implications of both mechanisms are
752 that $\delta^{138/134}Ba_{in}$ could be lower than the measured average sediment residue value (< 0
753 ‰). However, mass balance constraints requires that such isotope effects become
754 muted with increase weathering congruency. The implications for $\delta^{138/134}Ba_{in}$ being
755 lower than average residue $\delta^{138/134}$Ba are considered in context of the wider Ba
756 isotope systematics in section 6.3.
757
758 *6.2 Evaluation of constraints on F_{out}, $\delta^{138/134}Ba_{out}$ and $\delta^{138/134}Ba_{sp}$*
759
760 Constraining F_{out}, $\delta^{138/134}Ba_{out}$ and $\delta^{138/134}Ba_{sp}$ requires that the neo-formed
761 secondary phase Ba budget of river SPM samples can be quantitatively partitioned
762 from Ba associated with primary minerals. Here we propose that sequential leaching
763 steps 1 (1 M NH_4Cl) and 2 (5 mM HH) represent the sum of neo-formed secondary
764 phase Ba pool of the SPM samples. Combined, these leaching steps contain 5 to 31 %
765 (median 10 %) of the SPM Ba budgets (Fig. 4). These leaching steps are interpreted
766 as being dominated by Ba hosted in the exchange pool, with minor potential
767 contributions from Ba hosted in metal oxyhydroxide lattices (Supplementary
768 Information). The remaining Ba budget of the SPM samples is dominated by the
769 residue fraction (62 to 93%; median 86%), with negligible amounts of Ba hosted in
770 carbonates (primary and/or secondary) (Supplementary Information). It is assumed
771 that the residue fraction is dominated by Ba hosted in primary minerals (silicates and

772 potentially some marine barite), however, the importance of Ba hosted in the lattices
773 of neo-formed phyllosilicate minerals and structurally bound within organic matter is
774 unclear based on interpretation of the sequential leaching procedure results alone.
775 The importance of Ba hosted in organic matter in the SPM samples is
776 estimated by multiplying their particulate organic carbon (POC) concentrations by the
777 average plant Ba/C ratio of 0.2 μmol/g reported by Reimann et al. (2001) (eqn. 17)
778
779 $\text{Organic hosted Ba} = \text{POC} \times \text{Ba/C}_{\text{plants}}$ (eqn. 17)
780
781 The importance of Ba hosted in secondary phyllosilicates is estimated by multiplying
782 the concentration of SPM that is <2μm ($[\text{SPM}]_{<2\mu m}$: derived from grain size
783 distribution data) by the mean Ba concentration determined for the clay reference
784 samples of 0.37 μmol/g (eqn. 18).
785
786 $\text{Phyllosilicate hosted Ba} = [\text{SPM}]_{<2\mu m} \times [\text{Ba}]_{\text{Clay}}$ (eqn. 18)
787
788 Based on these estimates, phyllosilicate and organic-hosted Ba transported in these
789 river systems represent <14 and <1.6% respectively compared to $[\text{Ba}]_{sp}$ (sum of
790 leaching steps 1 and 2) and dissolved Ba fluxes (Fig. 9). These values are subject to
791 large uncertainty but likely overestimate the neo-formed Ba fraction associated with
792 these phases. Firstly, eqn. 18 assumes that the <2 μm fraction of the SPM load is
793 entirely composed of secondary phyllosilicates which is unlikely to be true. Secondly,
794 a significant fraction of the POC and secondary phyllosilicates transported in large
795 rivers are not formed within the current weathering cycle but are instead derived from
796 the erosion of sedimentary rocks (representing primary minerals in this case)

797 (Dellinger et al., 2014). For this reason, we suggest that the partitioning of Ba
798 between the dissolved and exchange pools dominate the budget of critical zone Ba,
799 with negligible Ba incorporation secondary mineral lattices and organic matter (Fig.
800 1). This justifies the use of data for sequential leaching procedure steps 1 and 2 for
801 constraining F_{out}, $\delta^{138/134}Ba_{out}$ and $\delta^{138/134}Ba_{sp}$.
802
803 *6.3 The Ba isotope systematics of the Irrawaddy and Salween River basins*
804
805 Our results reveal systematic links between riverine erosional dynamics, Ba
806 flux partitioning (f_{diss}) and isotope systematics consistent with those predicted by the
807 mass balance framework (section 2). Both f_{diss} and $\delta^{138/134}Ba_{out}$ systematically
808 decrease with increasing SPM concentration (Fig. 8). As f_{diss} tends towards 0,
809 corresponding to SPM concentrations > 1 g/L, $\delta^{138/134}Ba_{out}$ converges towards
810 $\delta^{138/134}Ba_{in}$ (Fig. 8). This is indicative of steady state conditions with respect to storage
811 of Ba in the critical zone secondary phase reservoirs ($F_{acc} = 0$) within these
812 catchments during conditions of high erosional output fluxes. In turn, this is consistent
813 with the similar values of $\delta^{138/134}Ba_{sp}$ and $\delta^{138/134}Ba_{in}$, which implies that $f_{diss\text{-}ss} \approx 0$ in
814 these catchments (Fig. 6; eqn. 8), although see further discussion below. These
815 conditions broadly align with estimates of annually averaged SPM concentrations for
816 the Irrawaddy at Pyay and the Salween at Hpa-An of 0.9 ± 0.2 and 1.1 ± 0.5 g/L
817 (Baronas et al., 2020), representing the best available constraint on the long-term
818 erosional balance in this region (i.e. the SPM concentration likely corresponding to
819 $f_{diss\text{-}ss}$).
820 Decreases in river SPM concentration relative to annual averaged values are
821 associated with systematic increases both f_{diss} (relative to a $f_{diss\text{-}ss} \approx 0$) and of

822 $\delta^{138/134}Ba_{out}$ (relative to $\delta^{138/134}Ba_{in} \approx 0$ ‰) (Fig. 8). This is indicative of the
823 accumulation of lighter Ba isotopes within critical zone secondary phase reservoirs in
824 the upstream catchment area (i.e. $F_{acc} > 0$; eqn. 7; eqn. 10), interpreted to reflect the
825 growth of the exchangeable Ba pool in up-stream soils due to chemical weathering
826 inputs of Ba (and other base cations) exceeding exports via erosion and leaching (Fig.
827 1). These dynamics are systematically linked to known perturbations to the river
828 catchments' erosional dynamics. Namely seasonal decreases in erosion relative to
829 dissolved fluxes in the dry season compared to the monsoon season and samples from
830 the dammed sub-catchments (Fig. 3). Lower SPM fluxes during the dry season
831 correspond to higher f_{diss} and $\delta^{138/134}Ba_{out}$. The highest values of f_{diss} and $\delta^{138/134}Ba_{out}$
832 correspond to samples from the three dammed sub-catchments of the Irrawaddy River
833 basin (Shweu, Mytinge and Mu) sampled during the monsoon season. These samples
834 feature the lowest SPM concentrations of the dataset. These observations are
835 interpreted to reflect the accumulation of eroded material within the reservoirs behind
836 these dams, sequestering lighter Ba isotopes on the associated exchange pool.
837 The systematic changes in $\delta^{138/134}Ba_{out}$ as a function of f_{diss} arise because
838 $\delta^{138/134}Ba_{diss}$ and $\delta^{138/134}Ba_{sp}$ do not themselves systematically vary with f_{diss} (Fig. 8).
839 In turn, this observation is consistent with the conditions of the critical zone behaving
840 as a zero-dimensional batch reactor with respect to Ba isotopes. The observation of
841 reasonably constant $\delta^{138/134}Ba_{sp}$ measured for river SPM at locations throughout the
842 river catchment broadly supports the assumption of a lack of spatial variance in this
843 parameter within the critical zone (but see below). Lack of systematic change in
844 $\delta^{138/134}Ba_{diss}$ and $\delta^{138/134}Ba_{sp}$ with f_{diss} is consistent with batch reaction conditions (i.e.
845 no evidence of Rayleigh distillation effects). These parameters, however, do exhibit
846 some variability that is independent of f_{diss}. This largely reflects variations in $\Delta_{diss\text{-}sp}$ of

between 0.10 to 0.37 ‰ (eqn. 6; Fig. 6). This likely reflects compositional differences in the secondary phases in the river SPM that host the exchange pool (phyllosilicates, Fe-oxyhydroxides, organic matter), which are known to be associated with variable $\Delta_{diss\text{-}sp}$ for dissolved-exchange pool Ba partitioning within the range observed in this study (Knight et al., 2024b).

A small but important inconsistency between the data and the mass balance framework is the observation that average $\delta^{138/134}Ba_{sp}$ (0.02± 0.02 ‰; mean ± 2SE, n = 18) is slightly higher than the average of the SPM residues used to constrain $\delta^{138/134}Ba_{in}$ (-0.03± 0.03 ‰; mean ± 2SE, n = 19) (Fig. 6). This difference is statistically significant at the 95% confidence level (one tailed t-test; t-stat (2.63) > t-crit (1.70); p = 0.01). Given the direction of $\Delta_{diss\text{-}sp}$ ($\delta^{138/134}Ba_{diss} > \delta^{138/134}Ba_{sp}$), the mass balance framework requires that $\delta^{138/134}Ba_{sp}$ must be less than or equal to, but not greater than, $\delta^{138/134}Ba_{in.}$ A higher $\delta^{138/134}Ba_{sp}$ than $\delta^{138/134}Ba_{in}$ (coupled with a positive $\Delta_{diss\text{-}sp}$) results in a physically unfeasible negative value for $f_{diss\text{-}ss}$ (eqn. 8). For example, using $\delta^{138/134}Ba_{in}$ of -0.03 ± 0.03 ‰, $\delta^{138/134}Ba_{sp}$ of 0.02 ± 0.02 ‰ and $\Delta_{diss\text{-}sp}$ of 0.23 ± 0.04 ‰ (mean ± 2SE) yields a $f_{diss\text{-}ss}$ of -0.21 ± 0.15 (2σ). Note that if $\delta^{138/134}Ba_{in}$ was in fact lower that the average river sediment residue values, due to an isotope fractionation accompanying chemical weathering (section 6.1), this discrepancy would be even larger.

There are two possible explanations to account for the fact that $\delta^{138/134}Ba_{sp}$ is slightly higher than $\delta^{138/134}Ba_{in}$. Firstly, there could be missing sink of isotopically light Ba within the critical zone shifting $\delta^{138/134}Ba_{sp}$ of river exports to higher values. Our data for the clay reference samples suggests that secondary phyllosilicate minerals feature $\delta^{138/134}$Ba values too high (0.02 to 0.22 ‰) to be a plausible missing sink. Biomass, however, is known to preferentially incorporate lighter Ba isotopes

872 (Bullen and Chadwick et al., 2016). Erosional exports of Ba hosted in biomass are
873 evaluated to be negligible in our study area (Fig. 9; section 6.2), but the preferential
874 uptake of lighter Ba isotopes into living biomass could conceivably shift soil
875 exchange pools to higher $\delta^{138/134}Ba$ than $\delta^{138/134}Ba_{in}$. While this explanation is
876 possible, it is difficult to more rigorously assess due to a current lack of understanding
877 of cycling of Ba isotopes internally within the critical zone.
878 The second possible explanation for the slight discrepancy between $\delta^{138/134}Ba_{sp}$
879 and $\delta^{138/134}Ba_{in}$ is that our estimate of $\delta^{138/134}Ba_{in}$ based on the river sediment residue
880 data is biased towards lower values. This explanation is supported by our data for the
881 river sediment residue fractions. The grain-size dependence of residue $\delta^{138/134}Ba$
882 means that our sampled population is prone to bias from the true catchment wide
883 average $\delta^{138/134}Ba$ of un-weathered parent rock material due to hydrodynamic sorting
884 (section 6.1). In particular, the winnowing of finer grain size fractions from bank
885 sands will bias them towards lower $\delta^{138/134}Ba$. Exclusion of bank sands from the river
886 sediment residue population results in an average $\delta^{138/134}Ba$ residue value (-0.01± 0.03
887 ‰; mean ± 2SE, n = 11) that is identical to that of $\delta^{138/134}Ba_{sp}$ at a 95% confidence
888 level (one tailed t-test; t-stat (1.45) < t-crit (1.74); p = 0.08). Combining this
889 constraint on $\delta^{138/134}Ba_{in}$ with $\delta^{138/134}Ba_{sp}$ (0.02± 0.02 ‰; mean ± 2SE, n = 18) and
890 $\Delta_{diss\text{-}sp}$ (0.23± 0.04 ‰; mean ± 2SE, n = 15) yields a $f_{diss\text{-}ss}$ of -0.13 ± 0.16 (2σ). While
891 the mean of this $f_{diss\text{-}ss}$ is still a physically unfeasible negative value, the upper 95%
892 confidence interval of this constraint is now positive (0.04).
893 The discrepancy between $\delta^{138/134}Ba_{in}$ and $\delta^{138/134}Ba_{sp}$ highlights an important
894 consideration for the practical application of the mass balance framework and the
895 need for further research into the partitioning of Ba isotopes among different
896 components of the critical zone. However, overall, the systematic links between

erosional dynamics (SPM concentrations), Ba flux partitioning (f_{diss} -$f_{diss\text{-}ss}$) and Ba isotope systematics ($\delta^{138/134}Ba_{out}$ - $\delta^{138/134}Ba_{in}$) provide validation for the application of the mass balance framework.

6.4 Quantifying imbalances in critical zone CEC budgets

The isotope mass balance framework is applied to quantify catchment wide imbalances in CEC budgets of the Irrawaddy and Salween river basins using data from Pyay and Hpa An (Table 2). These sites feature the full range of data required for this calculation and have been sampled under a range of seasonally varying hydrological conditions (Fig. 3). As described above, increases in SPM concentrations between low (February 2018) to peak (August 2018) discharge conditions result in a decline in $\delta^{138/134}Ba_{out}$ towards $\delta^{138/134}Ba_{in}$ (Fig. 10ab). Higher $\delta^{138/134}Ba_{out}$ relative to $\delta^{138/134}Ba_{in}$ during low flow conditions are interpreted to reflect the accumulation of isotopically light Ba in the exchange pools of the upstream critical zone (positive F_{acc}). During peak discharge conditions at Hpa An (Salween River), $\delta^{138/134}Ba_{out}$ is within uncertainty of $\delta^{138/134}Ba_{in}$, consistent with $F_{acc} = 0$ (Fig. 10bd). However, during peak discharge conditions at Pyay (Irrawaddy River) $\delta^{138/134}Ba_{out}$ is just outside of uncertainty from $\delta^{138/134}Ba_{in}$, indicating that $F_{acc} > 0$ (Fig. 10ac). These isotopic variations are used to calculate F_{acc}/F_{out} (eqn. 7) (Fig. 10cd).

Due to concerns over bias in the sampled river sediment residue $\delta^{138/134}Ba$ by hydrodynamic sorting (section 6.3), $\delta^{138/134}Ba_{in}$ is constrained as the average $\delta^{138/134}Ba$ of the upper continental crust (0.00± 0.04 ‰; Nan et al. 2018) (Table 2). For $\delta^{138/134}Ba_{sp}$, we take the mean (±2SE) of the entire dataset to best represent the average isotope composition of Ba stored in the exchangeable reservoir of the critical

zone in this region. Uncertainties on $\delta^{138/134}Ba_{out}$, $\delta^{138/134}Ba_{sp}$ and $\delta^{138/134}Ba_{in}$ are propagated using Monte Carlo simulations (n = 100,000) (Fig. 10cd). Given that the $f_{diss\text{-}ss}$ of these catchments is close to 0, with $\delta^{138/134}Ba_{sp} \approx \delta^{138/134}Ba_{in}$, the mass balance framework only has sensitivity for quantifying $F_{acc} > 0$ (accumulation of Ba within upstream exchange pools) (Fig. 2). As $\delta^{138/134}Ba_{in} - \delta^{138/134}Ba_{sp}$ (and $f_{diss\text{-}ss}$) tends towards 0, F_{acc}/F_{out} tends towards infinity (eqn. 10). Therefore, it is only possible to place minimum constraints on F_{acc}/F_{out} in this region of the mass balance framework. We take the 5th percentile of F_{acc}/F_{out} from the Monte Carlo simulations as this minimum constraint. An exception being the August 2018 sampling period at Hpa An, where $\delta^{138/134}Ba_{out} - \delta^{138/134}Ba_{in}$ is within uncertainty of 0 so that minimum F_{acc}/F_{out} is set to 0 (Fig. 10d). These minimum F_{acc}/F_{out} values are then multiplied by F_{out} to quantify minimum absolute F_{acc} values. Finally, β_{Ba} values (eqn. 15) are used to convert these Ba accumulation fluxes to catchment wide rates of changing CEC.

Minimum values of F_{acc}/F_{out} range between 4.1 and 0 and systematically decrease between low and high discharge conditions at both Pyay (to 0.9) and Hpa An (to 0) (Fig. 10cd, Table 2). These dynamics show that under low discharge conditions the majority of Ba released by chemical weathering reactions is retained within the exchange pool critical zone storage reservoir. At higher discharge conditions, large attendant increases in erosional outputs results in a higher proportion of Ba chemical weathering inputs being exported from the catchment. These results demonstrate the utility of this isotope mass balance framework to gain quantitative insight into the couplings between hydrology, chemical weathering and erosion.

During peak discharge conditions (August 2018), the Ba isotopic data indicates that the Salween River catchment is at steady state with respect to exchange pool elemental storage, with F_{acc}/F_{out}, and consequently CEC rate of change, within

947 uncertainty of 0 (Fig. 10, Table 2). At Pyay, however, absolute F_{acc} and CEC rates of
948 change are higher during peak discharge (8.4 ± 0.7 mol/s and 35 ± 5 meq/m^2/year)
949 than low discharge conditions (1.3 ± 0.1 mol/s and 5.5 ± 0.8 meq/m^2/year). This is
950 because although the relative magnitude of F_{acc} decreases (F_{acc}/F_{out}) at Pyay declines
951 by a factor of 4.6, F_{out} increases by a factor 29 between low discharge and high
952 discharge conditions.
953 Geomorphological differences between the two river catchments may explain
954 the observed differences in the seasonal dynamics of their CEC balance. The Salween
955 River catchment features limited floodplain area and therefore is expected to have
956 limited deposition of its SPM load during peak discharge conditions. By contrast, the
957 Irrawaddy River catchment features extensive floodplain areas that become active
958 during peak floodplain conditions. A large component of the Irrawaddy River SPM
959 load is expected to be deposited in these floodplains regions, which can explain the
960 high rates of CEC accumulation quantified by the isotope mass balance approach
961 during the monsoon season. These floodplains host key agricultural activities that
962 rely on the seasonal deposition of fertile river sediment (Taft and Evers, 2016). The
963 quantified accumulation of CEC during the peak discharge conditions therefore
964 represents a quantitative estimate on the net gain in soil quality within floodplain
965 soils. Sediment transport within the Irrawaddy River catchment has yet to be
966 significantly perturbed by dam construction, although future hydroelectric dam
967 developments have been proposed (Taft and Evers, 2016). The construction of such
968 dams would disrupt the deposition of fertile sediment to the floodplain. The results
969 described above demonstrate the utility of the isotope mass balance framework to
970 place quantitative constraints on the impact of dam construction on downstream
971 floodplain soil quality.

7. Conclusions

Barium isotope systematics of river samples can be used to place quantitative constraints on rates of changing base cation storage within the exchange pool reservoir of the upstream river catchment area. The utility of this isotope system to this end is enabled by the dominance of Ba partitioning between the dissolved and exchange pool reservoirs within the critical zone, accompanied by a stable isotope fractionation. This tool can be applied to gain fundamental, quantitative, constraints on the balance between chemical weathering and erosion rates at a river catchment scale. For example, it can provide quantitative constraints on the couplings between hydroclimate, chemical weathering and erosion rates, and on the net rates of secondary phase accumulation in floodplains. Such applications have relevance for constraining land degradation rates due to human perturbations to soil erosion. In river catchments dominated by erosional outputs, as studied here, this approach has sensitivity for constraining changes in the net accumulation of CEC within river floodplains driven by dam construction. However, river catchments draining lowland regions that are dominated by dissolved outputs, it is hypothesized that this approach would have sensitivity for constraining net depletions of CEC driven by land-use changes and/or climate change.

CRediT authorship contribution statement

Luke Bridgestock: Conceptualization, Funding acquisition, Investigation, Visualization, Writing – original draft. **Emily Stevenson:** Investigation, Data Curation, Writing – review & editing. **J. Jotautas Baronas:** Investigation, Data

Curation, Writing – review & editing. **Alasdair Knight:** Investigation, Writing – review & editing. **Harold J. Bradbury:** Resources, Writing – review & editing. **Alexandra V. Turchyn:** Resources, Writing – review & editing. **Edward T. Tipper:** Supervision, Funding acquisition, Writing – review & editing.

Declaration of competing interests

The authors declare that they have no known competing financial interests or personal relationships that could have appeared to influence the work reported in this paper.

Data availability

Data are available at the HydroShare repository:
https://doi.org/10.4211/hs.3521fe4163b24a968af76eed44309043

Acknowledgements

This research was supported by a Leverhulme Trust Early Career Fellowship (ECF-2019-049) backed by the Isaac Newton Trust awarded to L.B. ETT and JB were funded by NERC grant NE/P011659/1 that supported the collection of the field samples. Tim Elliot (University of Bristol) is thanked for supplying the barium double spike used in this study. Heye Freymuth (University of Cambridge) is thanked for assistance in the calibration of the barium double spike. Marie-Laure Bagard and Heye Freymuth are thanked for assistance in running the laboratories at the Department of Earth Sciences, University of Cambridge.

Appendix A. Supplementary Material.

The following is available in the Supplementary Material file: S.1 Derivation of mass balance equations for critical zone secondary phase elemental balances, S.2 Sequential leaching procedure and interpretation of results in terms of phase partitioning, S.3 Details of the analytical methods for Ba isotope measurements, S.4. Rain sample results and S.5 Suspended particulate material depth profiles for Pyay and Hpa An.

References

An, Y-J., Li, X. and Zhang, Z-F., 2020, Barium isotopic compositions in thirty-four geological reference materials analysed by MC-ICP-MS, *Geostandards and geoanalytical research*, 44, 183-199, doi:10.1111/ggr.12299

Baronas, J. J., Stevenson, E. I., Hackney, C. R., Darby, S. E., Bickle, M. J., Hilton, R. G., Larkin, C. S., Parsons, D. R., Aung Myo Khaing and Tipper, E. T., 2020, Integrating suspended sediment flux in large alluvial river channels: Application of a synoptic Rouse-based model to the Irrawaddy and Salween Rivers, *Journal of Geophysical Research: Earth Surface,* 125, e2020JF005554, doi:10.1029/2020JF005554

Bhagwat, T., Hess, A., Horning, N., Khaing, N., Zaw Min Thein, Kyaw Moe Aung, Kyaw Htet Aung, Paing Phyo, Ye Lin Tun, Aung Htat Oo, Neil A., Win Myo Thu, Songer, M., LaJeunesse Connette, K., Bernd, A., Huang, Q., Connette, G. and Leimgruber, P., 2017, Losing a jewel – Rapid declines in Myanmar's intact forests from 2002-2014, *PLoS ONE*, 12, e0176364, doi:10.1371/journal.pone.0176364

Bouchez, J., Gaillardet, J., France-Lanord, C., Maurice, L. and Dutra-Maia, P., 2011, Grain size control of river suspended sediment geochemistry: Clues from Amazon River depth profiles, *Geochemistry, Geophysics, Geosystems,* 12, doi:10.1029/2010GC003380

Bouchez, J., von Blanckenburg, F. and Schuessler, J. A., 2013, Modeling novel stable isotope ratios in the weathering zone, *American Journal of Science*, 313, 267-308, doi:10.2475/04.2013.01

Bridgestock, L., Henderson, G. M., Holdship, P., Khaing, A. M., Naing, T. T., Myint, T. A., Htun, W. W., Khant, W., Thu, W. M., Chi, M. A. N., Baronas, J. J., Tipper, E., Chapman, H. and Bickle, M., 2022, Dissolved trace element concentrations and fluxes in the Irrawaddy, Salween, Sittaung and Kaladan Rivers, *Science of the total environment*, 841, 156756, doi:10.1016/j.scitotenv.2022.156756

1063 Bridgestock, L., Nathan, J., Paver, R., Hsieh, Y-T., Porcelli, D., Tanzil, J., Holdship,
1064 P., Carrasco, G., Annammala, K. V., Swarzenski, P. W. and Henderson, G. M., 2021,
1065 Estuarine processes modify the isotope composition of dissolved riverine barium
1066 fluxes to the ocean, *Chemical Geology,* 579, 120340,
1067 doi:10.1016/j.chemgeo.2021.120340
1068
1069 Bullen, T. and Chadwick, O., 2016, Ca, Sr and Ba stable isotopes reveal the fate of
1070 soil nutrients along a tropical climosequence in Hawaii, *Chemical Geology*, 422, 25-
1071 45, doi:10.1016/j.chemgeo.2015.12.008
1072
1073 Cao, Z., Roa, X., Yu, Y., Siebert, C. Hathorne, E. C., Liu, B., Wnag, G., Lian, E.,
1074 Wang, Z., Zhang, R., Gao, L., Wei, G., Yang, S., Dai, M. and Frank, M., 2021, Stable
1075 barium isotope dynamics during estuarine mixing, *Geophysical Research Letters,*
1076 doi:10.1029/2021GL095680
1077
1078 Chapman, H., Bickle, M., San Hla Thaw, Hrin Nei Thiam, 2015, Chemical fluxes
1079 from time series sampling of the Irrawaddy and Salween Rivers, Myanmar, *Chemical*
1080 *Geology*, 401, 15-27, doi:10.1016/j.chemgeo.2015.02.012
1081
1082 Charbonnier, Q., Bouchez, J., Gaillardet, J. and Gayer, E., 2020, Barium stable
1083 isotopes as a fingerprint of biological cycling in the Amazon River basin,
1084 *Biogeosciences*, 17, 5989-6015, doi:10.5194/bg-17-5989-2020
1085
1086 Charbonnier, G., Bouchez, J., Gaillardet, J., Gayer, E. and Porder, S., 2022a, A global
1087 imbalance in potassium and barium river export: the result of biological uptake?,
1088 *Geochemical Perspectives Letters*, 21, 32-36, doi:10.7185/geochemlet.2214
1089
1090 Charbonnier, Q., Bouchez, J., Gaillardet, J., Calmels, D. and Dellinger, M., 2022b,
1091 The influence of black shale weathering on riverine barium isotopes, Chemical
1092 Geology, 594, 120741, doi:10.1016/j.chemgeo.2022.120741
1093
1094 Chen, D., Li, X., Saito, Y., Liu, J. P., Duan, Y., Liu, S. and Zhang, L., 2020, Recent
1095 evolution of the Irrawaddy (Ayeyarwady) delta and the impacts of anthropogenic
1096 activities: A review and remote sensing survey, *Geomorphology*, 365, 107231,
1097 doi:10.1016/j.geomorph.2020.10723
1098
1099 Ćirić, V., Prekop, N., Šeremešić, S., Vojnov, B., Pejić, B., Radovanović, D. and
1100 Marinković, D., 2023, The implication of cation exchange capacity (CEC) assessment
1101 for soil quality management and improvement, *Agriculture and Forestry*, 69, 113-
1102 133, doi:10.17707/AgricultForest.69.4.08
1103
1104 Dellinger, M., Gaillardet, J., Bouchez, J., Calmels, D., Galy, V., Hilton, R. G.,
1105 Louvat, P. and France-Lanord, C., 2014, Lithium isotopes in large rivers reveal the
1106 cannibalistic nature of modern continental weathering and erosion, *Earth and*
1107 *Planetary Science Letters*, 401, 359-372, doi:10.1016/j.epsl/2014.05.061
1108
1109 Dellinger, M., Gaillardet, J., Bouchez, J., Calmels, D., Louvat, P., Dosseto, A., Gorge,
1110 C., Alanoca, L., and Maurice, L., 2015, Riverine Li isotope fractionation in the
1111 Amazon River basin controlled by the weathering regimes, *Geochimica et*
1112 *Cosmochimica Acta*, 164, 71-93, doi:10.1016/j.gca.2015.04.042

Deng, G., Kang, J., Nan, X., Li, Y., Guo, J., Ding, X. and Huang, F., 2021, Barium isotope evidence for crystal-melt separation in granitic magma reservoirs, *Geochimica et Cosmochimica*, 292, 115-129, doi:10.1016/j.gca.2020.09.027

Dong, X., Hu, X., Li, G., Garzanti, E., Najman, Y., Liang, W., Tian, Y. and Wang, J., 2025, Accelerated erosion and sediment fluxes in the Ayeyarwady River due to anthropogenic activities, *Journal of Geophysical Research: Earth Surface,* 130, e2024JF008204

Drescher, G. L., Slaton, N. A., Roberts, T. L. and Smartt, A. D., 2024, Soil texture and organic matter prediction using Mehlich-3 extractable nutrients, *Agrosystems*, 7, e10461doi:10.1002/agg2.20461

Furuichi, T., Win, Z. and Wasson, R. J., 2009, Discharge and suspended sediment transport in the Ayeyarwady River, Myanmar: Centennial and decadal changes, *Hydrological Processes*, 23, 1631-1641, doi:10.1002/hyp.7295

Gaillardet, J., Dupré, B., Louvat, P. and Allègre, C. J., 1999, Global silicate weathering and CO_2 consumption rates deduced from the chemistry of large rivers, *Chemical Geology*, 159, 3-30

Garcia-Ruiz, J., Begueria, S., Nadal-Romero, E., González-Hidalgo, J. C., Lana-Renault, N. and Sanjuán, Y., 2015, A meta-analysis of soil erosion rates across the world, *Geomorphology*, 239, 160-173, doi:10.1016/j.geomorph.2015.03.008

Garzanti, E. Wang, J-G., Vezzoli, G. and Limonta, M., 2016, Tracing provenance and sediment fluxes in the Irrawaddy River basin (Myanmar), *Chemical Geology*, 440, 73-90, doi:10.1016/j.chemgeo.2016.06.010

Geymann B. M., Ptacek J. L., LaVigne M. and Horner T. J., 2019, Barium in deep-sea bamboo corals: Phase associations, barium isotopes, and prospects for paleoceanography, *Earth and Planetary Science Letters*, 525, 115751, doi:10.1016/j.epsl.2019.115751

Gong, Y., Zeng, Z., Cheng, W., Lu, Y., Zhang, L., Yu, H. and Huang, F., 2020, Barium isotopic fractionation during strong weathering of basalt in a tropical climate, *Environment International*, doi:10.1016/j.envint.2020.105896

Gou, L-F., Jin, Z., Galy, A., Gong, Y-Z., Nan X-Y., Jin, C., Wang, X-D., Bouchez, J., Cai, H-M., Chen, J-B., Yu, H-M. and Huang, F., 2020, Seasonal riverine barium isotopic variations in the middle Yellow River: Sources and fractionation, *Earth and Planetary Science Letters*, 531, doi:10.1016/j.epsl.2019.115990

Grill, G., Lehner, B., Thieme, M., Geenen, B., Tickner, D., Antonelli, F., Babu, S., Borrelli, P., Cheng, L., Crochetiere, H., Ehalt Macedo, H., Filgueiras, R., Goichot, M., Higgins, J., Hogan, Z., Lip, B., McCalin, M. E., Meng, J., Mulligan, M., Nilsson, C., Olden, J. D., Opperman, J. J., Petry, P., Reidy, Liermann, C., Sáenz, L., Salinas-Rodriguez, S., Schelle, P., Schmitt, R. J. P., Snider, J., Tan, F., Tockner, K., Valdujo,

P. H., van Soesbergen, A. and Zarfl, C., 2019, Mapping the world's free-flowing rivers, *Nature,* 569, 215-221, doi:10.1038/s41586-019-1111-9

Horner T. J., Pryer H. V., Nielsen S. G., Crockford P. W., Gauglitz J. M., Wing B. A. and Ricketts R. D., 2017, Pelagic barite precipitation at micromolar ambient sulfate, *Nature Communications*, 8, 1242, doi:10.1038/s41467-017-01229-5

Ito A. and Wagai, R., 2017, Global distribution of clay-size minerals on land surface for biogeochemical and climatological studies, *Scientific Data*, 4, 170103, doi:10.1038/sdata.2017.103

Jasechko S., Kirchner J. W., Welker J. M. and McDonnell J. J., 2016, Substantial proportion of global streamflow less than three months old, *Nature Geoscience*, 9, 126-129, doi:10.1038/ngeo2636

Jobbágy, E. G., and Jackson, R. B., 2001, The distribution of soil nutrients with depth: Global patterns and the imprint of plants, *Biogeochemistry*, 53, 51-77

Knight, A. C. G., Stevenson, E. I., Bridgestock, L., Baronas, J. J., Knapp, W. J., Adhikari, B. R., Andermann, C. and Tipper, E. T., 2024a, The impact of adsorption-desorption reactions on the chemistry of Himalayan rivers and the quantification of silicate weathering rates, *Earth and Planetary Science Letters*, 641, 118814, doi:10.1016/j.epsl.2024.118814

Knight, A. C. G., Tipper, E. T. Tipper, Bradbury, H. J., Turchyn, A. V., Andermann, C., Freymuth, H., Elliott, T., Bridgestock, L., 2024b, Experimental constraints on barium isotope fractionation during adsorption–desorption reactions: Implications for weathering and erosion tracer applications, Geochimica et Cosmochimica Acta, 384, 194-212, doi:10.1016/j.gca.2024.08.016

Larkin, C. S., Piotrowski, A. M., Hindshaw, R. S., Bayon, G., Hilton, R. G., Baronas, J. J., Dellinger, M., Wang, R., Tipper, E. T., 2021, Constraints on the source of reactive phases in sediment from a major Arctic river using neodymium isotopes, Earth and Planetary Science Letters, 565, 116933, doi:10.1016/j.epsl.2021.116933

Latrubesse, E. M., Park, E. and Kästner, K., 2021, The Ayeyarwady River (Myanmar): Washload transport and its global role among rivers in the Anthropocene, *PLoS ONE*, 16(5), e0251156, doi:10.1371/journal.pone.0251156

Li, Z. and Fang, H., 2016, Impacts of climate change on water erosion: A review, *Earth-Science Reviews*, 163, 94-117, doi:10.1016/j.earscirev.2016.10.004

Milliman, J. D., and Farnsworth, K. L. 2011, River discharge to the coastal ocean: a global synthesis, Cambridge University Press

Miyazaki T., Kimura J-I. and Chang Q., 2014, Analysis of stable isotope ratios of Ba by double spike standard-sample bracketing using multiple-collector inductively coupled plasma mass spectrometry, *J. Anal. At. Spectrom.,* 29, 483-490, doi:10.1039/c3ja50311a

Montgomery, D. R., 2007, Soil erosion and agricultural sustainability, *Proceedings of the National Academy of Sciences*, 104, 13268-13272, doi:10.1073/pnas.0611508104

Nan X-Y, Yu H-M., Rudnick R. L., Gaschnig R. M., Xu J., Li W-Y., Zhang Q., Jin Z-D, Li X-H. and Huang F., 2018, Barium isotopic composition of the upper continental crust, *Geochimica and Cosmochimica Acta*, 233, 33-49, doi:10.1016/j.gca.2018.05.004

Nan. X., Wu, F., Zhang, Z., Hou, Z., Haung, F. and Yu, H., 2015, High-precision barium isotope measurements by MC-ICP-MS, *J. Anal. At. Spectrom.,* doi:10.1039/c5ja00166h

Olsson, L., Barbosa, H., Bhadwal, S., Cowie, A., Delusca, K., Flores-Renteria, D., Hermans, K., Jobbagy, E., Kurz, W., Li, D., Sonwa, D. J. and Stringer, L., 2019, Land degradation. In: Climate Change and Land: an IPCC special report on climate change, desertification, land degradation, sustainable land management, food security and greenhouse gas fluxes in terrestrial ecosystems, doi:10.1017/9781009157988.006

Reimann, C., Koller, F., Frengstad, B., Kashulina, G., Niskavaara, H. and Englmaier, P., 2001, Comparison of the element composition in several plant species and their substrate from a 1 500 000-km^2 area in Northern Europe, *Science of the Total Environment*, 278, 87-112

Salmivaara, A., Kummu, M., Keskinen, M. and Varis, O., 2013, Using global datasets to create environmental profiles for data-poor regions: A case from the Irrawaddy and Salween River basins, *Environmental Management*, 51, 897-911, doi:10.1007/s00267-013-0016-x

Sposito, G., Skipper, N. T., Sutton, R., Park, S-H., Soper, A. K., and Greathouse, J. A., 1999, Surface geochemistry of the clay minerals, *Proceedings of the National Academy of Sciences*, 96. 3358-3364

Stevenson, E. I., Burton, K. W., Parkinson, I. J., James, R. H., Kisakürek, B., Tipper, E. and Bickle, M., 2025, Calcite dissolution-reprecipitation reactions are a key control on the Sr/Ca, Mg/Ca, and δ^{88}Sr compositions of Himalayan River water, *American Journal of Science*, 324, doi:10.2475/001c.124202

Syvitski, J., Ángel, J. R., Saito, Y., Overeem, I., Vorosmarty, C. J., Wang, H. and Olago, D., 2022, Earth's sediment cycle during the Anthropocene, *Nature Reviews Earth & Environment,* doi:10.1038/s43017-021-00253-w

Taft, L. and Evers, M., 2016, A review of current and possible future human-water dynamics in Myanmar's river basins. *Hydrology and Earth System Sciences*, 20, 4913-4928, doi:10.5194/hess-20-4913-2016

Tang, L. and Sparks, D. L., 1993, Cation-exchange kinetics on montmorillonite using pressure-jump relaxation, *Soil Science Society of American Journal,* 57, 42-46

Teppen, B. J. and Miller, D. M., 2006, Hydration energy determines isovalent cation exchange selectivity by clay minerals, *Soil Science Society of American Journal,* 70, 31-40, doi:10.2136/sssaj2004.0212

Tessier, A., Campbell, P. G. C. and Bisson, M., 1979, Sequential extraction procedure for the speciation of particulate trace metals, *Analytical Chemistry*, 51, 844-851

Tian, L-L., Zeng, Z., Nan, X-Y., Yu, H-M. and Haung, F., 2019, Determining Ba isotopes of barite using the Na_2CO_3 exchange reaction and double-spike method by MC-ICP-MS, *J. Anal. At. Spectrom.,* 34, 1459, doi:10.1039/c9ja00064j

Tieman Z. G., Stewart B. W., Capo R. C., Phan T., Lopano C. and Hakala J. A., 2020, Barium isotopes track the source of dissolved solids in produced water from the unconventional Marcellus shale gas play, *Environmental Science and Technology,* 54**,** 4275-4285, doi:10.1021/acs.est.0c00102

Tipper, E. T., Lemarchand, E., Hindshaw, R. S., Reynolds, B. C. and Bourdon, B., 2012, Seasonal sensitivity of weathering processes: Hints from magnesium isotopes in a glacial stream, *Chemical Geology*, 312-313, 80-92, doi:10.1016/j.chemgeo.2021.04.002

Tipper, E. T., Stevenson, E. I., Alcock, V., Knight, A. C., Baronas, J. J., Hilton, R. G., Bickle, M. J., Larkin, C. S., Feng, L., Relph, K. E. and Hughes, G., 2021, Global silicate weathering flux overestimated because of sediment–water cation exchange. *Proceedings of the National Academy of Sciences*, *118*(1), e2016430118, doi:10.1073/pnas.2016430118

Tripathy, G. R, Mishra, S., Danish, M. and Ram, K., 2019, Elevated barium concentrations in rain water from east-coast of India: role of regional lithology, *Journal of Atmospheric Chemistry*, 76, 59-72, doi:10.1007/s10874-019-9387-6

van Zuilen K., Nagler T. F. and Bullen T. D., 2016, Barium isotopic compositions of geological reference materials, *Geostandards and Geoanalytical Research*,40, 543-558, doi:10.1111/ggr.12122

Vogt, C., Lauterjung, J. and Fischer, R. X., 2002, Investigation of the clay fraction (<2 μm) of the clay minerals society reference clays, *Clays and clay minerals*, 50, 388-400

von Blanckenburg, F., Schuessler, J. A., Bouchez, J., Frings, P. J., Uhlig, D., Oelze, M., Frick, D. A., Hewawasam, T., Dixon, J. and Norton, K., 2021, Rock weathering and nutrient cycling along an erodosequence, *American Journal of Science*, 321, 1111-1163, doi:10.2475/08.2021.01

1310 **Table 1**, Definitions of terms used in the mass balance framework

Term	Definition
F_{acc}	Flux of element accumulating in critical zone secondary phase reservoirs (moles/time).
F_{in}	Flux of element supplied to critical zone secondary phase reservoirs by chemical weathering reactions and atmospheric deposition (moles/time).
F_{out}	Flux of element out of critical zone secondary phase reservoirs by river dissolved and suspended particulate material loads (moles/time).
F_{cw}	Flux of element supplied to critical zone secondary phase reservoirs by chemical weathering reactions. Component of F_{in} (moles/time).
F_{atm}	Flux of element supplied to critical zone secondary phase reservoirs by atmospheric deposition. Component of F_{in} (moles/time).
F_{diss}	Flux of element out of critical zone secondary phase reservoirs by river dissolved loads. Component of F_{out} (moles/time).
F_{er}	Flux of element out of critical zone secondary phase reservoirs by river suspended sediment loads. Component of F_{out} (moles/time).
$\delta^{xx}X_{in}$	Stable isotope composition of F_{in} (‰)
$\delta^{xx}X_{out}$	Stable isotope composition of F_{out} (‰)
$\delta^{xx}X_{sp}$	Stable isotope composition of critical zone secondary phases (‰)
$\delta^{xx}X_{diss}$	Stable isotope composition of river dissolved loads (‰)
f_{diss}	Fraction of F_{out} via river dissolved loads
$f_{diss\text{-}ss}$	Fraction of F_{out} via river dissolved loads under the condition that $F_{acc} = 0$
f_{er}	Fraction of F_{out} via river suspended sediment loads
$\Delta_{diss\text{-}sp}$	Isotope fractionation between dissolved and secondary phases
CEC	Cation exchange capacity
β_{Ba}	Fraction of CEC supported by Ba^{2+} ions

1311

1312

1313

1314

1315

1316

1317

1318

1319

1320

1321

Table 2, Input and output values for calculation of upstream CEC rates of change for the Irrawaddy River at Pyay and Salween River at Hpa An under different hydrological conditions

	Irrawaddy at Pyay			Salween at Hpa An	
	February 2018	**August 2018**	**May 2019**	**August 2018**	**May 2019**
Input Parameters					
Discharge (m^3/s)	3000	32100	5300	14300	2700
SPM (g/L) [a]	0.06 (n = 1)	0.99 (n =3)	0.17 (n =2)	3.76 (n =3)	0.41 (n =2)
f_{diss} [a]	0.79 ± 0.01	0.18 ± 0.01	0.40 ± 0.01	0.19 ± 0.14	0.53 ± 0.14
F_{out} (mol/s) [b]	0.33 ± 0.02	9.4 ± 0.8	0.64 ± 0.05	14 ± 10	0.9 ± 0.4
$\delta^{138/134}Ba_{out}$ (‰)[c]	0.18 ± 0.03	0.08 ± 0.03	0.11 ± 0.03	0.02 ± 0.04	0.09 ± 0.04
$\delta^{138/134}Ba_{in}$ (‰)[d]			0.00 ± 0.04		
$\delta^{138/134}Ba_{sp}$ (‰)[e]			0.02 ± 0.02		
β_{Ba} [f]		0.0033 ± 0.0005		0.0026 ± 0.0004	
Area (km^2) [g]		436,500		282,300	
Output Parameters					
F_{acc}/F_{out} [h]	4.1	0.9	1.9	0	1.1
F_{acc} (mol/s)[i]	1.3 ± 0.1	8.4 ± 0.7	1.22 ± 0.09	0	1.0 ± 0.4
CEC rate of change ($meq/m^2/year$)[j]	5.5 ± 0.8	35 ± 5	5.0 ± 0.7	0	9 ± 3

[a] Average value based on multiple depth profile SPM samples. Uncertainty on f_{diss} values based on the 2SD of results from depth SPM samples collected in the August 2018 sampling period that features n = 3 for both Pyay and Hpa An (Supplementary Fig. 9).

[b] Calculated using eqn. 12 with uncertainty based on propagation of errors on discharge (± 6%; Baronas et al., 2020), $[Ba]_{diss}$ (±5%) and SPM × $[Ba]_{sp}$. The latter was taken as 2SD of the depth profile SPM samples (n = 3) collected in the August 2018 sampling period (±6% for Pyay and ±86% for Hpa An).

[c] Calculated using eqn. 5, with uncertainty based on propagation of errors on f_{diss}, $\delta^{138/134}Ba_{diss}$ and $\delta^{138/134}Ba_{sp}$.

[d] Average $\delta^{138/134}Ba$ of the upper continental crust as constrained by Nan et al. (2018)

[e] Mean $\delta^{138/134}Ba_{sp}$ of the entire dataset presented in this study (± 2SE, n = 18).

[f] Mean values (± 2SE) for the β_{Ba} determined for all SPM samples featuring sequential leaching data from the Pyay (n = 5) and Hpa An (n = 5) sampling locations respectively.

[g] Calculated using a digital elevation model (Baronas et al., 2020)

[h] 5th percentile of values from Monte Carlo error propagation model (Fig. 10). Exception being for Hpa An in August 2018 which is set to 0.

[i] Calculated by multiplying F_{out} by the 5th percentile of F_{acc}/F_{out}. Uncertainty is propagated from the error on F_{out}.

[j] Calculated by scaling F_{acc} by β_{Ba} with uncertainty propagated from the errors on two parameters, and normalizing by catchment area.

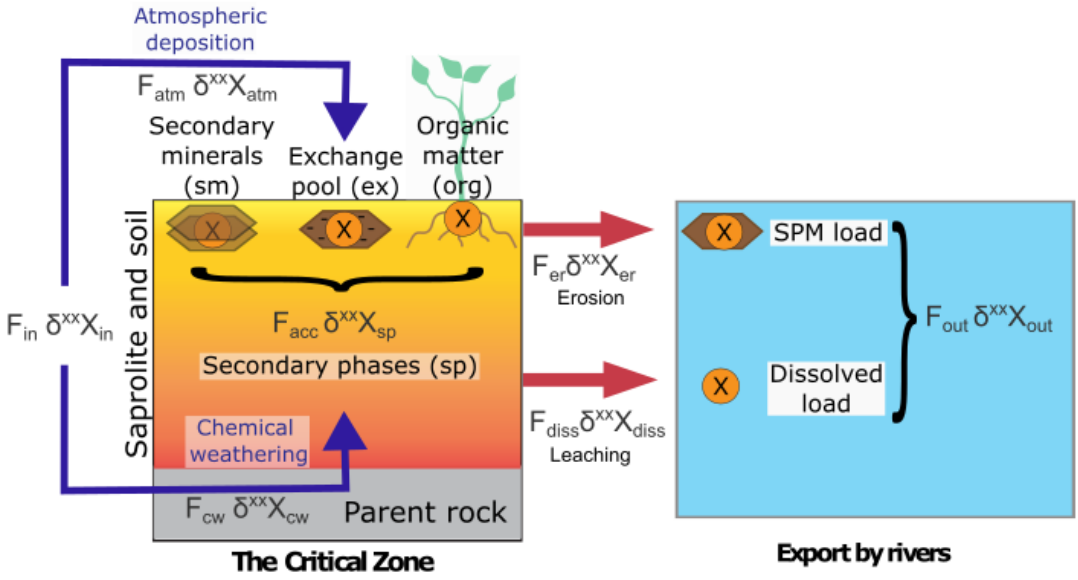

Figure 1, Schematic of the fluxes and storage reservoirs considered in the mass balance framework. Fluxes are denoted by 'F' and stable isotope compositions by '$\delta^{xx}X$'. See Table 1 for a full list of definitions of the terms. SPM – suspended particulate material.

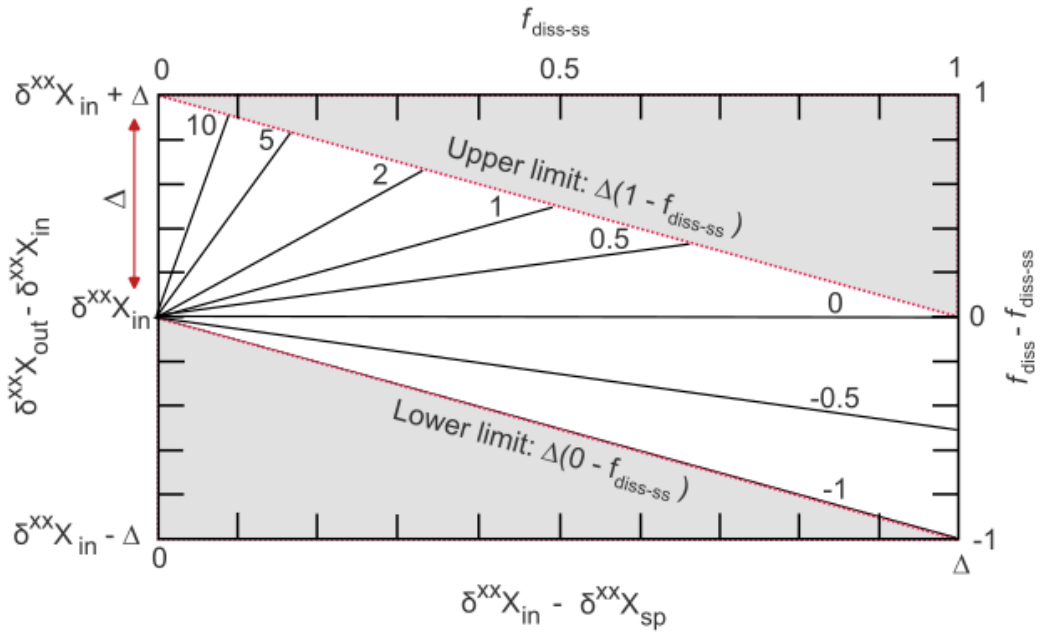

1357

1358 **Figure 2,** Limits on the isotope mass balance framework for quantifying F_{acc}/F_{out} as a

1359 function of $f_{diss-ss}$ (eqn. 10). Δ denotes the isotope fractionation between dissolved and

1360 secondary phase reservoirs ($\Delta_{diss-sp}$; eqn. 6). Solid black lines denote contours of

1361 constant F_{acc}/F_{out} with values labeled by adjacent numbers (-1 to 10).

1362

1363

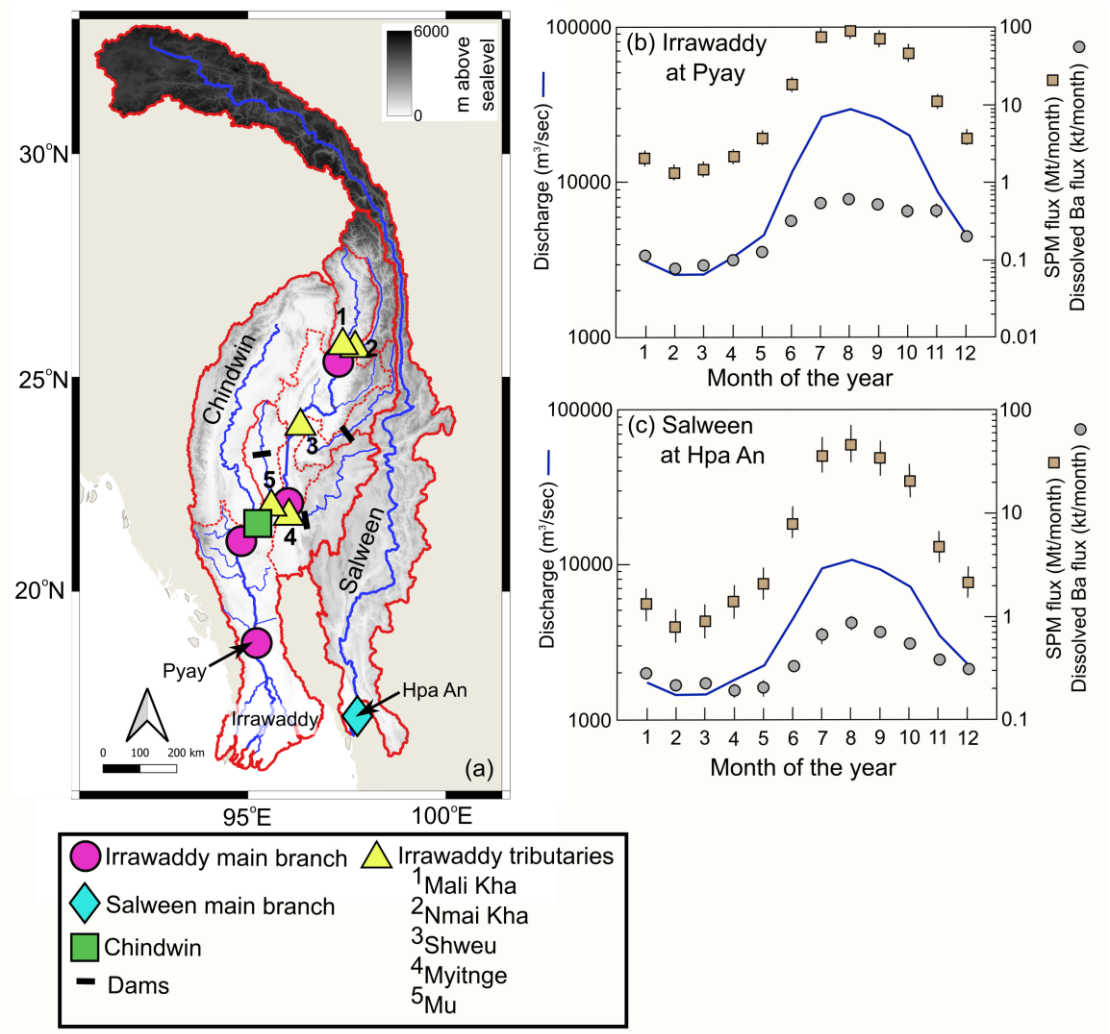

Figure 3, Sample locations and study area characteristics. Panel (a); map of study area with sample locations. Red lines denote river catchment boundaries. Panels (b) and (c) show monthly averaged discharge, SPM (Baronas et al., 2020) and dissolved Ba fluxes (Bridgestock et al., 2022) for the Irrawaddy at Pyay and Salween at Hpa An respectively. Uses the geodetic system WGS 84.

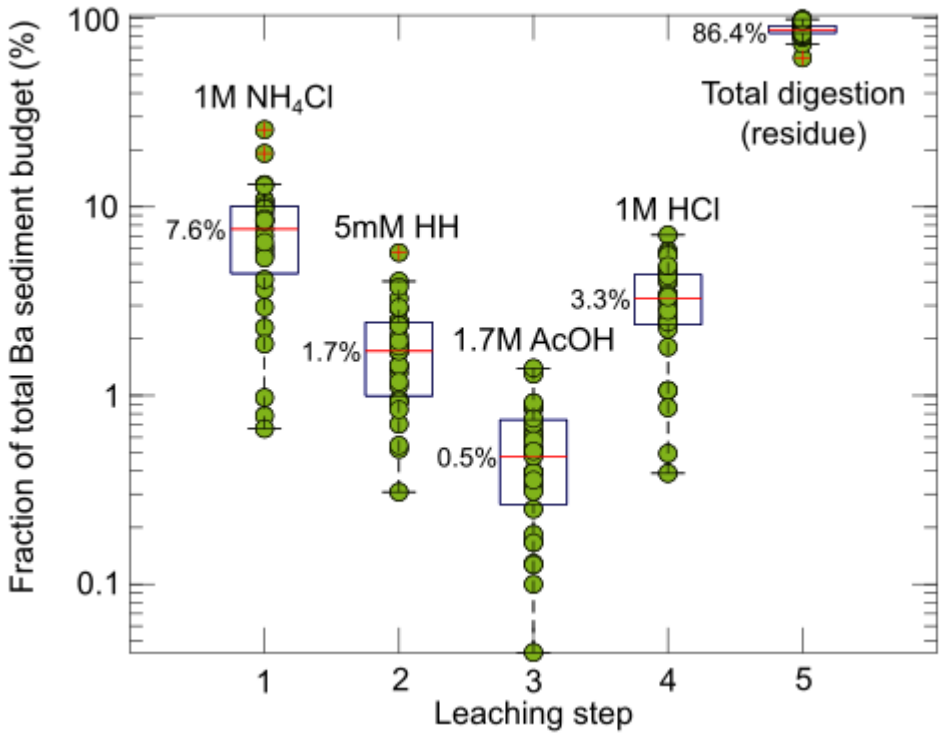

1371

1372 **Figure 4,** Partitioning of Ba between sequential leaching steps of riverine sediment

1373 samples. Red bars and corresponding numbers denote the median values for each

1374 leaching step. AcOH - acetic acid.

1375

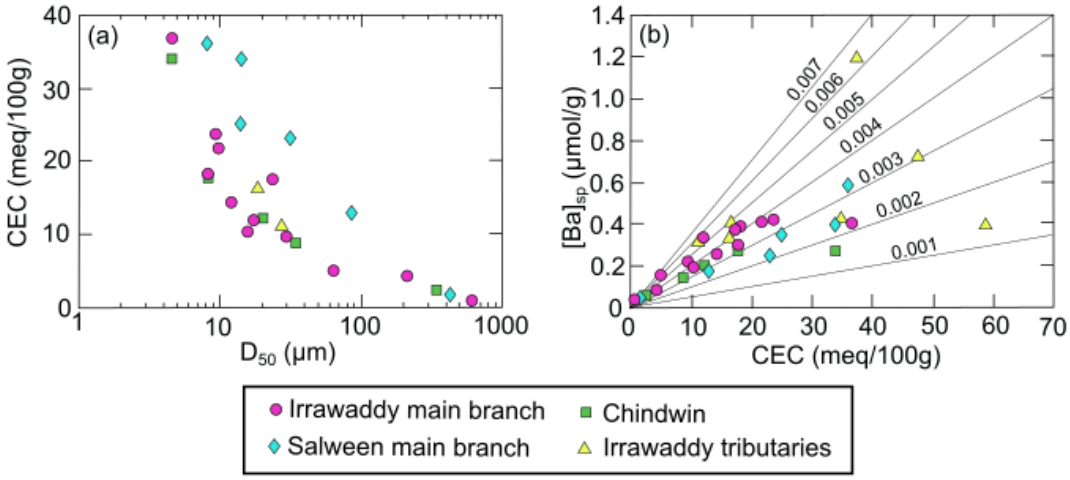

1376

1377 **Figure 5,** Relationships between sediment grain size (D_{50}), cation exchange capacity

1378 (CEC) and exchangeable Ba concentrations ($[Ba]_{sp}$). The black lines in panel (b)

1379 denote contours of β_{Ba}.

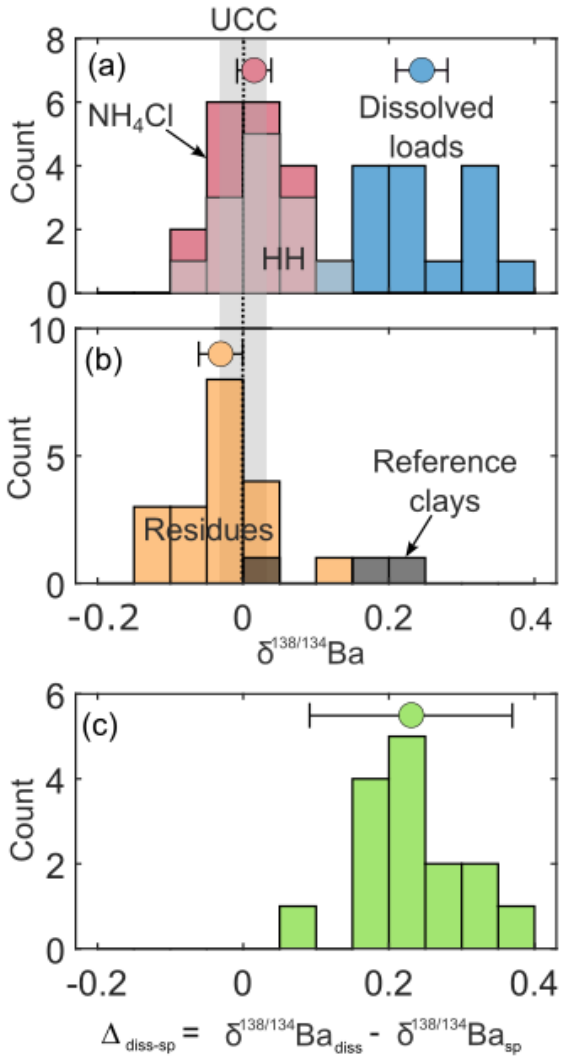

Figure 6, Histograms of $\delta^{138/134}$Ba values of the river water, sediment leachate fractions and reference clays. The vertical dashed line and grey shaded area in panel (a) and (b) denotes the composition of the upper continental crust (UCC, mean ± 2SE; Nan et al., 2018). Circles and error bars denote the mean ± 2SE of the populations. Panel (c) shows the offsets between of $\delta^{138/134}Ba_{diss}$ and $\delta^{138/134}Ba_{sp}$ of paired river water-SPM samples, with the circle and error bar denoting the mean ± 2SD of the population.

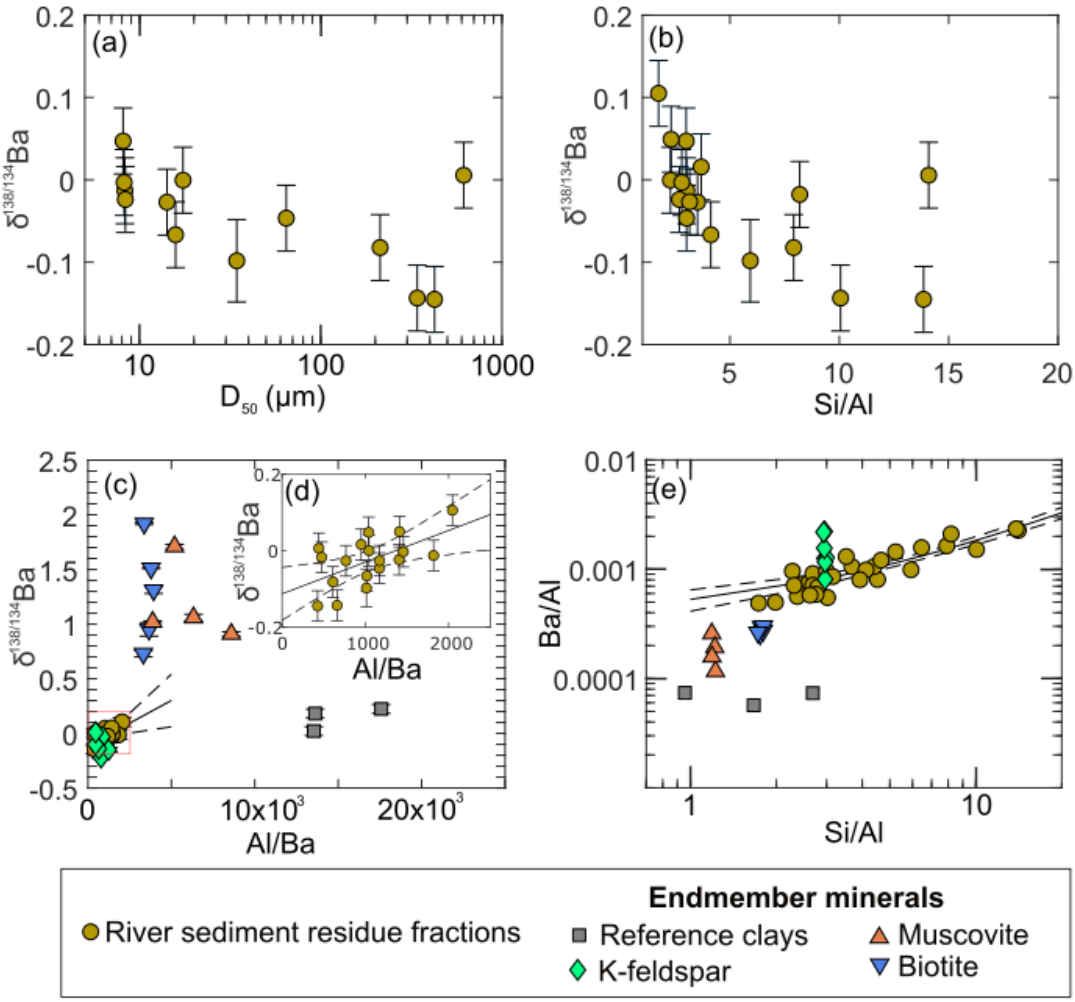

Figure 7, Relationships between $\delta^{138/134}$Ba values of river sediment residue fractions with grain size (D_{50}) and residue elemental ratios. Dashed line and grey shaded area denote the mean ± 2SE of the river sediment residue $\delta^{138/134}$Ba. Panel (c) and (e) include data for the reference clay samples (KGa-2, SWy-2 and ISCz-1; this study) and important silicate minerals for hosting Ba (K-feldspar, muscovite, biotite; Deng et al., 2021). The inset, panel (d), displays only the river sediment residue data on a zoomed in region of panel (c) denoted by the red box. Solid blank lines in panels (c), (d) and (e) are linear regressions through the river sediment residue data, with the black dashed lines denoting 95% confidence intervals. Note that two endmember mixing in panels (c), (d) and (e) is linear.

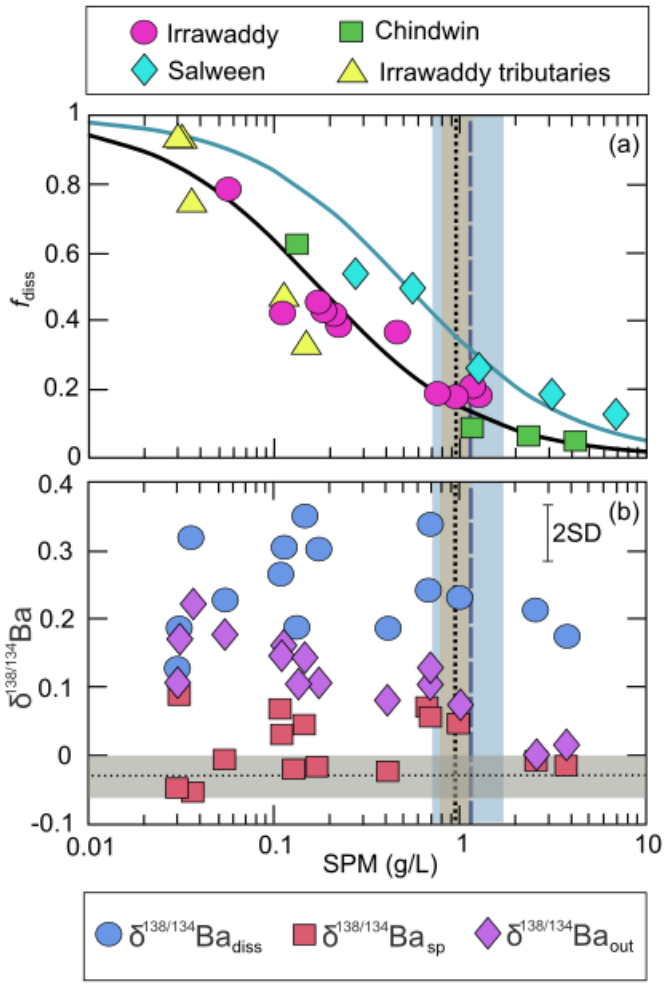

Figure 8, Relations between f_{diss} and $\delta^{138/134}$Ba values of riverine output components with SPM concentrations. In panel (a), the solid black line is f_{diss} as a function of SPM calculated using eqn. 13 and the mean $[Ba]_{diss}$ (0.05 µmol/L) and $[Ba]_{sp}$ (0.29 µmol/g) of Irrawaddy and Chindwin river samples. The solid blue line is f_{diss} as a function of SPM calculated using eqn. 13 and the mean $[Ba]_{diss}$ (0.18 µmol/L) and $[Ba]_{sp}$ (0.35 µmol/g) of Salween River samples. In panel (b), the dashed line and grey shaded area denote the mean ± 2SE of the river sediment residue $\delta^{138/134}$Ba. The vertical black dashed line and brown shaded area denotes the annually averaged SPM concentration of the Irrawaddy at Pyay (0.9 ± 0.2 g/L; Baronas et al., 2020). The vertical blue dashed line and blue shaded area denotes the annually averaged SPM concentration of

1413 the Salween at Hpa An (1.1 ± 0.5 g/L; Baronas et al., 2020). The error bar displays

1414 analytical uncertainty of the $\delta^{138/134}$Ba values of ± 0.04 ‰.

1415

1416

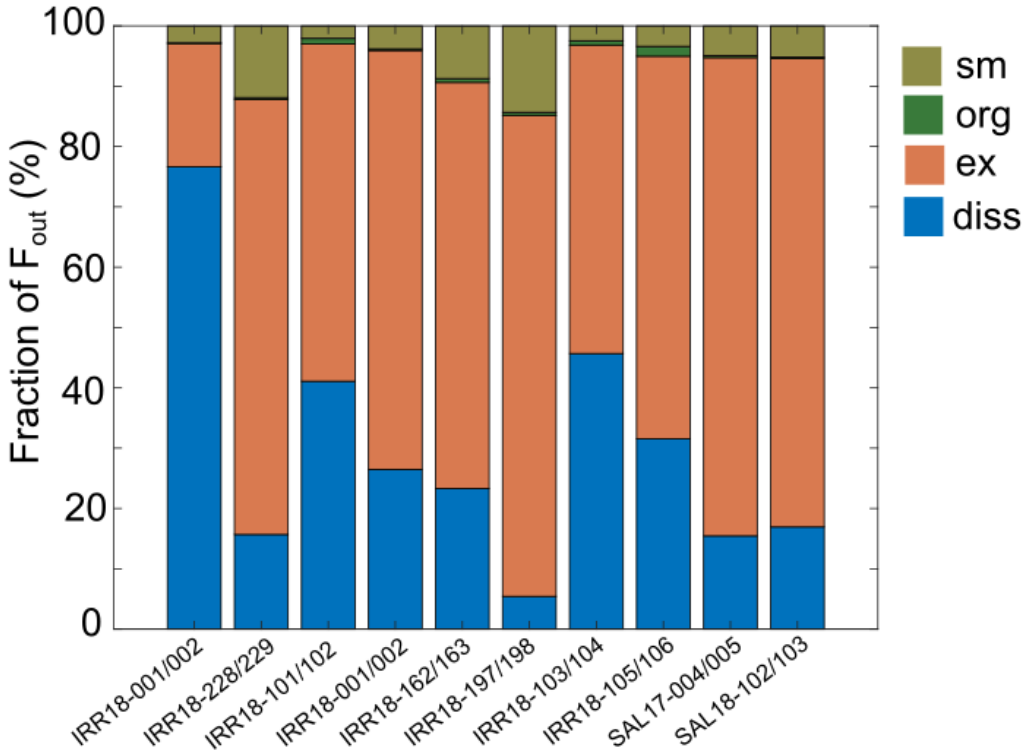

1417

1418 **Figure 9,** Partitioning of Ba between riverine output (F_{out}) components, included the

1419 river dissolved load (diss) and secondary phases in river SPM loads; exchange pool

1420 (ex), organic matter (org) and secondary mineral lattices (sm). Sample identification

1421 codes for the water/suspended sediment samples are labelled along the x-axis.

1422

1423

1424

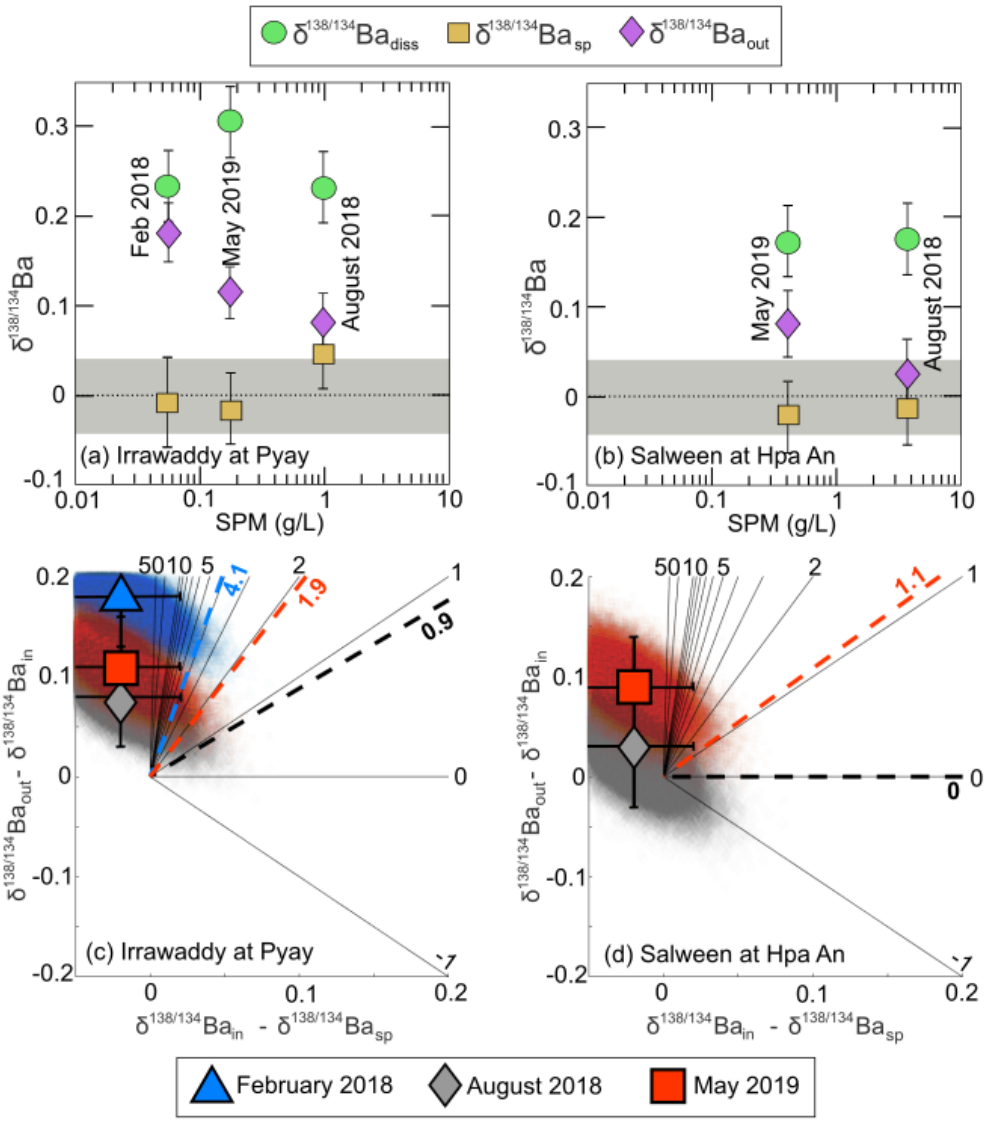

Figure 10, Seasonal changes in the Ba isotope systematics of the Irrawaddy and Salween rivers. Panels (a) and (b) show changes in $\delta^{138/134}Ba_{diss}$, $\delta^{138/134}Ba_{sp}$ and $\delta^{138/134}Ba_{out}$ as a function of SPM concentrations under different hydrological conditions (low discharge; February 2018, rising discharge; May 2019, peak discharge; August 2018). The dashed line and grey shaded area denote the mean ± 2SE of the upper continental crust (Nan et al., 2018) taken to reflect $\delta^{138/134}Ba_{in}$. Panels (c) and (d) show plots of $\delta^{138/134}Ba_{out}$ - $\delta^{138/134}Ba_{in}$ vs $\delta^{138/134}Ba_{in}$ - $\delta^{138/134}Ba_{sp}$. Solid black contours and associated numbers denote constant values of F_{acc}/F_{out}. Colored shaded areas show the error ellipses from Monte Carlo simulations (n =

100,000). Dashed colored lines show the F_{acc}/F_{out} values of the 5th percentile of each population of Monte Carlo simulation results.

Supplementary Material for

Erosion-driven changes in soil cation exchange capacity quantified using barium isotopes

Luke Bridgestock[1,2*], Emily Stevenson[1,$], J. Jotautas Baronas[1,3], Alasdair Knight[1,4], Harold J. Bradbury[1,5], Alexandra V. Turchyn[1] and Edward Tipper[1]

[1]Department of Earth Sciences, University of Cambridge, Downing Street, Cambridge, CB2 3EQ, UK

[2]School of Earth and Environmental Sciences, University of St Andrews, Bute Building, Queen's Terrace, St Andrews, KY16 9TS, UK

[3]Department of Earth Sciences, Durham University, Durham, DH1 3LE, County Durham, UK

[4]Department of Earth Sciences, University of Oxford, South Parks Road, Oxford, OX1 3AN, UK

[5]Department of Earth, Ocean and Atmospheric Sciences, University of British Columbia, Vancouver, British Columbia, Canada

[$] Now at GFZ Helmholtz-Zentrum für Geoforschung, 14473, Deutschland

*Corresponding author; ljb35@st-andrews.ac.uk

S1. Derivation of mass balance equations for critical zone secondary phase elemental balances

Equation 1 in the main article can be solved for F_{in} (eqn. S1):

$$F_{in} = F_{acc} + F_{out} \quad \text{(eqn. S1)}$$

The right-hand side of this equation (eqn. S1) can then be substituted into to eqn. 4 in the main article for F_{in} (eqn. S2):

$$\delta^{xx}X_{sp}\, F_{acc} = \delta^{xx}X_{in}\, (F_{acc} + F_{out}) - \delta^{xx}X_{out}\, F_{out} \quad \text{(eqn. S2)}$$

Expanding the brackets gives (eqn. S3):

$$\delta^{xx}X_{sp}\, F_{acc} = \delta^{xx}X_{in}\, F_{acc} + \delta^{xx}X_{in}\, F_{out} - \delta^{xx}X_{out}\, F_{out} \quad \text{(eqn. S3)}$$

Rearranging to have terms featuring F_{acc} on the left-hand side and terms featuring F_{out} on the right-hand side, and factorizing both sides gives (eqn. S4):

$$F_{acc}(\delta^{xx}X_{sp} - \delta^{xx}X_{in}) = F_{out}\, (\delta^{xx}X_{in} - \delta^{xx}X_{out}) \quad \text{(eqn. S4)}$$

Dividing by $(\delta^{xx}X_{sp} - \delta^{xx}X_{in})$ leads to (eqn. S5), equivalent to eqn. 7 quoted in the main article (after inversion of the terms in the bracket on the right-hand side):

$$F_{acc} = F_{out} \left(\frac{\delta^{xx}X_{in} - \delta^{xx}X_{out}}{\delta^{xx}X_{sp} - \delta^{xx}X_{in}}\right) \quad \text{(eqn. S5)}$$

Differences between $\delta^{xx}X_{sp}$ and $\delta^{xx}X_{in}$ (the dominator in eqn. 7 main article) arise over timescales similar too or greater than the residence time of element X in critical zone secondary phases. Over such timescales, the critical zone mass balance of element X can be assumed to approach steady state ($F_{acc} = 0$, with $F_{in} = F_{out}$) with this isotope mass balance given by (eqn. S6):

$$\delta^{xx}X_{in} F_{in} = \delta^{xx}X_{out} F_{out} = \delta^{xx}X_{diss} F_{diss} + \delta^{xx}X_{sp} F_{er} \quad \text{(eqn. S6)}$$

Normalizing the terms in eqn. S6 to F_{in} yields (eqn. S7):

$$\delta^{xx}X_{in} = \delta^{xx}X_{diss} f_{diss\text{-}ss} + \delta^{xx}X_{sp} (1 - f_{diss\text{-}ss}) \quad \text{(eqn. S7)}$$

Where $f_{diss\text{-}ss}$ is the fractional contribution of F_{diss} to F_{out} (F_{diss}/ F_{out}) when the system is at steady state ($F_{in}=F_{out}$, $F_{acc}=0$). Rearrangement of eqn. S7 leads to eqn. S8.

$$\delta^{xx}X_{in} - \delta^{xx}X_{sp} = f_{diss\text{-}ss} (\delta^{xx}X_{diss} - \delta^{xx}X_{sp}) \quad \text{(eqn. S8)}$$

Noting that $\delta^{xx}X_{diss} - \delta^{xx}X_{sp} = \Delta_{diss\text{-}sp}$ (eqn. 4 main article) we arrive at eqn. 8 (main article).

$$\delta^{xx}X_{in} - \delta^{xx}X_{sp} = f_{diss\text{-}ss} \Delta_{diss\text{-}sp} \quad \text{(eqn. 8, main article)}$$

The limits on $f_{diss\text{-}ss}$ are between 0 ($F_{diss} = 0$) and 1 ($F_{diss} = F_{out}$), so that $\delta^{xx}X_{in} - \delta^{xx}X_{sp}$ has the limits of 0 ($f_{diss\text{-}ss} = 0$) and $\Delta_{diss\text{-}sp}$ ($f_{diss\text{-}ss} = 1$).

Differences between $\delta^{xx}X_{out}$ and $\delta^{xx}X_{in}$ (the numerator in eqn. 7) arise due to short term imbalances between F_{in} and F_{out}. The isotope composition of the output flux ($\delta^{xx}X_{out}$) can be re-expressed in terms of its two flux components (eqn. 5, main article).

$$\delta^{xx}X_{out} - \delta^{xx}X_{in} = \delta^{xx}X_{diss} f_{diss} + \delta^{xx}X_{sp} (1 - f_{diss}) - \delta^{xx}X_{in} \quad \text{(eqn. S10)}$$

Which can be further rearranged into the following form:

$$\delta^{xx}X_{out} - \delta^{xx}X_{in} = \delta^{xx}X_{sp} - \delta^{xx}X_{in} + f_{diss}(\delta^{xx}X_{diss} - \delta^{xx}X_{sp}) \quad \text{(eqn. S11)}$$

Substituting in eqn. 8 (main article) for $\delta^{xx}X_{sp} - \delta^{xx}X_{in}$ and eqn. 6 (main article) for $\delta^{xx}X_{diss} - \delta^{xx}X_{sp}$, and factorizing we arrive at eqn. 9 in the main article:

$$\delta^{xx}X_{out} - \delta^{xx}X_{in} = \Delta_{diss\text{-}sp} (f_{diss} - f_{diss\text{-}ss}) \quad \text{(eqn. 9, main article)}$$

Substitution of eqn. 8 and 9 into eqn. 7 (main article) leads to (eqn. S12):

$$F_{acc} = F_{out} \left(\frac{\Delta_{diss-sp} (f_{diss} - f_{diss-ss})}{\Delta_{diss-sp} f_{diss-ss}} \right) \quad \text{(eqn. S12)}$$

Cancelling of $\Delta_{diss\text{-}sp}$ and rearrangement leads to eqn. 10 (main article):

$$\frac{F_{acc}}{F_{out}} = \left(\frac{f_{diss} - f_{diss-ss}}{f_{diss-ss}} \right) \quad \text{(eqn. 10, main article)}$$

Supplementary Table 1, Summary of certified reference material results for assessing the quality of river/rainwater cation and Si data.

Element	SLRS-6		SPS-SW2 10%	
	This study Mean ± 2SD (n)	Certified value	This study Mean ± 2SD (n)	Certified value
Ba nmol/L	104 ± 4 (11)	104 ± 3	179 ± 3 (9)	182 ± 1
Ca µmol/L	228 ± 9 (11)	219 ± 5	26 ± 1 (9)	25.0 ± 0.1
Mg µmol/L	95 ± 6 (11)	88 ± 2	8.5 ± 0.5 (9)	8.24 ± 0.04
Na µmol/L	115 ± 3 (11)	120 ± 3	44 ± 3 (9)	43.6 ± 0.2
K µmol/L	17 ± 1 (11)	17 ± 1	2.71 ± 0.1 (8)	2.56 ± 0.01
Sr nmol/L	432 ± 16 (11)	465 ± 4	269 ± 13 (9)	286 ± 1
Si µmol/L	88 ± 4 (11)	NA	18.4 ± 1 (9)	17.8 ± 0.1

SPS-SW2 10% denotes SPS-SW2 diluted by a factor of 10, with the quoted certified values also scaled by the same dilution factor.

S.2 Sequential leaching procedure and interpretation of results in terms of phase partitioning

S.2.1 Methodological details of the sequential leaching procedure

The sequential leaching procedure used to extract different phases within the riverine sediments is outlined in Supplementary Table 2.

Supplementary Table 2, Details of the sequential leaching procedure used to partition riverine sediment phases as previously described by Larkin et al., 2021. Conducted on ~0.4 g of dried sediment.

Step	Notes
(1) 16 ml 1M NH_4Cl Target phase: the exchange pool	Shaken by hand then ultrasonic bath for 20 minutes, then centrifuged to separate supernatant
(2) 10 ml HH Target phase: metal oxyhyr(oxides)	Shaken by hand then placed on shaker table for 1 hour, then centrifuged to separate supernatant. Sediment was then washed 3 times with 50ml milli-q water to removed residual Na sourced from the HH solution, with the supernatant separated by centrifugation
(3) 16ml 1.7M acetic acid Target phase: calcite and other carbonates	Placed in ultrasonic bath for 20 minutes, then shaken by hand, and placed on shaker table for 3 hours. Supernatant was then separated by centrifugation.
(4) 16ml 1M HCl Target phase: Dolomite and any remaining authigenic phases	Shaken by hand then placed on shaker table for ~12 hours. Supernatant was then separated by centrifugation.
(5) Loss on ignition followed by total digestion Target phase: Silicates	Dried residues were ignited at 950°C, with weighs before and after ignition recorded to quantify loss on ignition. The residues were then subjected to total digestion by fusion with lithium tetraborate/metaborate (1:4 ratio) before dissolution in 2.5 % HNO_3.

HH; 5mM hydroxylamine hydrochloride+ 3M Na-EDTA+1.5% acetic acid buffered to a pH of ~4 with NaOH

Centrifugation to separate supernatant between steps was conducted at between 4000 and 5000 revolutions per minute for 15 minutes

Reagent blanks for leaching steps 1 (1M NH_4Cl) and 2 (5mM HH) were 58 and 19 ng of Ba respectively, representing 0.2 to 3.8% and 0.2 to 0.75% of the Ba in these leachates. Reagent Ba blanks for other leaching steps were below the limits of detection.

S.2.2 Results of sequential leaching tests and their implications for interpreting Ba phase partitioning

1597 The results of sequential leaching procedures require careful interpretation
1598 regarding the phases they target for a given element. Leaching steps may extract
1599 elements from phases other than those targeted or may only partially extract the total
1600 elemental pool associated with the target phase. Below we provide detailed arguments
1601 regarding the interpretation of the phase associations of Ba sampled by the different
1602 leaching steps.
1603 Step 1 (1M NH_4Cl; Supplementary Table 2) intended to sample cations
1604 associated with the exchange pool (i.e. cations adsorbed to particle surfaces). This
1605 assumes that adsorbed cations are quantitatively displayed by NH_4^+ ions from the
1606 reagent without any dissolution of mineral phases. Dissolution of soluble mineral
1607 phases, notably carbonates (see Tipper et al., 2021), is however possible. It is also
1608 possible that the single 1M NH_4Cl leaching step employed in this study only partially
1609 extracts elements associated from exchange pool, due to incomplete displacement by
1610 NH_4^+ ions.
1611 Carbonate dissolution can be assessed using radiogenic Sr isotopes (Tipper et
1612 al., 2021). The exchange pools and corresponding river waters should have identical
1613 $^{87}Sr/^{86}Sr$ ratios, while carbonate dissolution will likely contribute Sr with a distinct
1614 isotope composition. The radiogenic Sr isotope composition of paired river water and
1615 exchange pool samples selected for Ba isotope analysis are identical, with the
1616 exceptions of samples IRR18_103/104 (Mali Kha) and SAL18_102/103 (Salween)
1617 (Supplementary Fig. 1). These results argue against carbonate dissolution impacting
1618 the 1M NH_4Cl leaching steps for the majority of the samples. In any case, carbonate
1619 dissolution should not significantly impact Ba in these extractions, as carbonates
1620 contain very low Ba contents (see below). This is supported by the similar
1621 exchanageble Ba concentrations of IRR18_103/104 (Mali Kha) and SAL18_102/103

(Salween) (0.26 and 0.25 µmol/g) compared to the other SPM samples (0.29 ± 0.18 µmol/g; mean ±1SD, n =25).

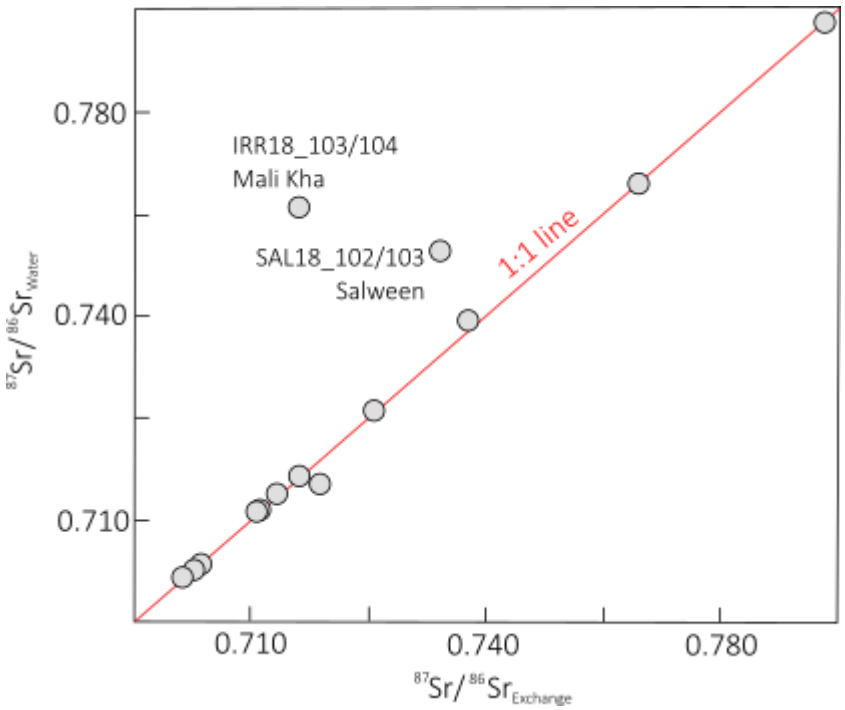

Supplementary Figure 1, Comparison of $^{87}Sr/^{86}Sr$ ratios for filtered river water and exchange pool extracts (1M NH_4Cl) for corresponding suspended sediments. Error bars are small than the symbol size (±0.000003 to 0.000039: 2SD).

To assess the how quantitative the single 1M NH_4Cl employed in this study is for extracting Ba (and other cations) from the exchange pool, three samples (IRR18-229, IRR18-230 and IRR18-184) were subjected to leaching with 3 repeat 1M NH_4Cl steps followed by the 5mM HH step. Supplementary Fig. 2 and 3 show comparisons of results of leaching procedures using 1 x 1M NH_4Cl step versus 3 x 1M NH_4Cl steps for these samples. Elemental concentrations agree within 10% for the first 1M NH_4Cl step of the two leaching procedures, exceptions being Na and K that agree within 15 to 20%. The quantity of element extracted decreases with each additional 1M NH_4Cl

step, with the first 1M NH_4Cl step extracting between 75% and 90% (~80% for Ba) of the total of all three 1M NH_4Cl steps. An exception to this is K, where the first 1M NH_4Cl extracts ~100% of the budget, due to K being below detection limits in most of the subsequent 1M NH_4Cl steps. The 5mM HH step following 3 x 1M NH_4Cl steps extracts 40% to 50% less than that following the single 1M NH_4Cl (Supplementary Fig. 2). The total elemental pools extracted by the two leaching procedures (1 x 1M NH4Cl + 5 mM HH versus 3 x 1M NH4Cl + 5 mM HH) agree within 15% for most elements. Sodium is excluded from this comparison because it was not measured in the 5mM HH leachates as the reagent contains NaOH.

The observations detailed above suggest that leaching using a single 1M NH_4Cl step extracts 75 to 90% of the cations hosted in the exchange pool. The remaining exchange pool cations (10 to 25% of the exchange pool budget) are extracted in step 2 of the leaching procedure (5 mM HH), and that ~50% of the cations (Ca, Mg, Sr, Ba, K) in the 5mM HH extractions are actually associated with the exchange pool rather than its intended target; metal oxyhyroxides (Supplementary Table 2).

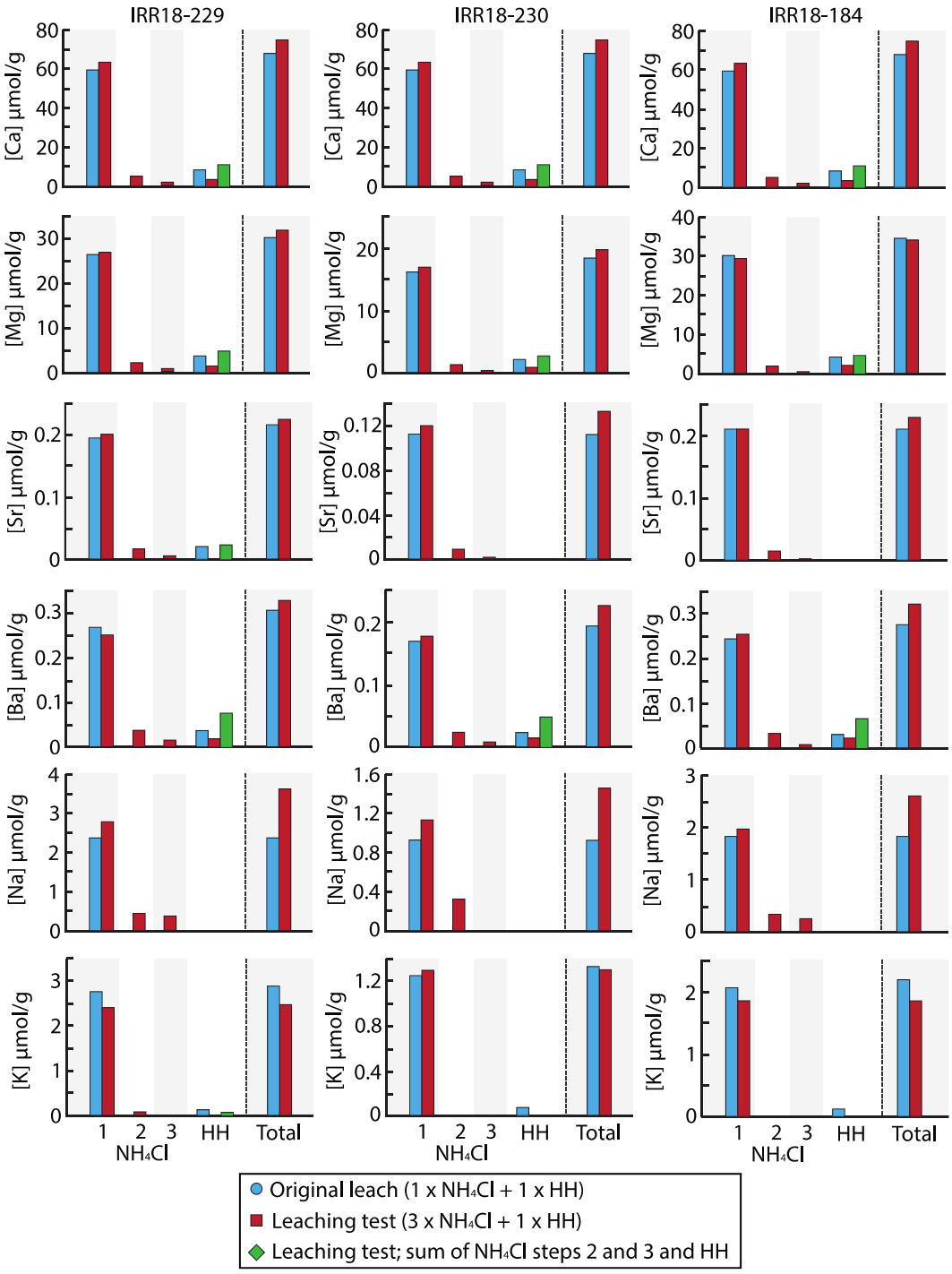

Supplementary Figure 2, Comparison of elemental results for procedures employing 1 x 1M NH_4Cl versus 3 x 1M NH_4Cl steps. Note that Na was not measured in the 5mM HH steps due to the reagent containing NaOH, and K is below detection in some of the sequential 1M NH4Cl and 5mM HH steps. The 'total' elemental pools are the sum of the elemental contents of all of the leaching steps of each procedure.

The $\delta^{138/134}Ba$ values of the first 1M NH_4Cl step of the two leaching procedures agree within analytical uncertainty (Supplementary Fig. 3). For samples IRR18-229 and IRR18-184, $\delta^{138/134}Ba$ values decrease systematically with sequential 1M NH_4Cl step, while no clear trend is observed for IRR18-230. The 5mM HH step in the 3 x 1M NH_4Cl procedure feature lower $\delta^{138/134}Ba$ values than those in the 1 x 1M NH_4Cl procedure. The $\delta^{138/134}Ba$ values of the total Ba pools extracted by the 2 procedures agree within analytical uncertainty, and are identical to those extracted during the 1st 1M NH_4Cl steps of both procedures.

Based on these observations, we take the combined Ba content and $\delta^{138/134}Ba$ value of the 1M NH_4Cl and 5mM HH steps to represent the neo-formed secondary phase Ba pool, which is interpreted to be dominated by the exchange pool (eqn. S13 and S14).

$$[Ba]_{sp} = [Ba]_{NH4Cl} + [Ba]_{HH} \quad \text{(eqn. S13)}$$

$$\delta^{138/134}Ba_{sp} = (\delta^{138/134}Ba_{NH4Cl} \times [Ba]_{NH4Cl} + \delta^{138/134}Ba_{HH} \times [Ba]_{HH})/ [Ba]_{sp} \quad \text{(eqn. S14)}$$

Where $[Ba]_{NH4Cl}$, $[Ba]_{HH}$ and $[Ba]_{sp}$ are the Ba concentration (μmol Ba per g of sediment) of the 1M NH_4Cl leachate, 5mM HH leachate and the secondary phase Ba pool respectively, and $\delta^{138/134}Ba_{NH4Cl}$, $\delta^{138/134}Ba_{HH}$ and $\delta^{138/134}Ba_{spx}$ are the $\delta^{138/134}Ba$ values of these components. For the SPM samples, $[Ba]_{sp}$ is 12 to 37% (mean of 16%) higher than the 1M NH_4Cl leachate, while $\delta^{138/134}Ba_{sp}$ differs by <0.03 ‰ compared to that of the 1M NH_4Cl leachates.

Out of 18 sediment samples with $\delta^{138/134}Ba_{NH4Cl}$ data, 5 have no $\delta^{138/134}Ba_{HH}$ data. Two of these (IRR18-231 and IRR18-187) have $\delta^{138/134}Ba_{HH}$ data for other

suspended sediment samples collected in the same depth profile (IRR18-229, IRR18-230 and IRR18-184), which was used to calculate their $\delta^{138/134}Ba_{sp}$ values. For IRR18-176 and IRR18-179, the average $\delta^{138/134}Ba_{HH}$ of the other samples of 0.02 ‰ was used to calculate $\delta^{138/134}Ba_{sp}$. Sample IRR18-017A has not data for either $[Ba]_{HH}$ or $\delta^{138/134}Ba_{HH}$. For this sample, $[Ba]_{sp}$ and $\delta^{138/134}Ba_{sp}$ were taken as those measured on the 1M NH_4Cl leachate.

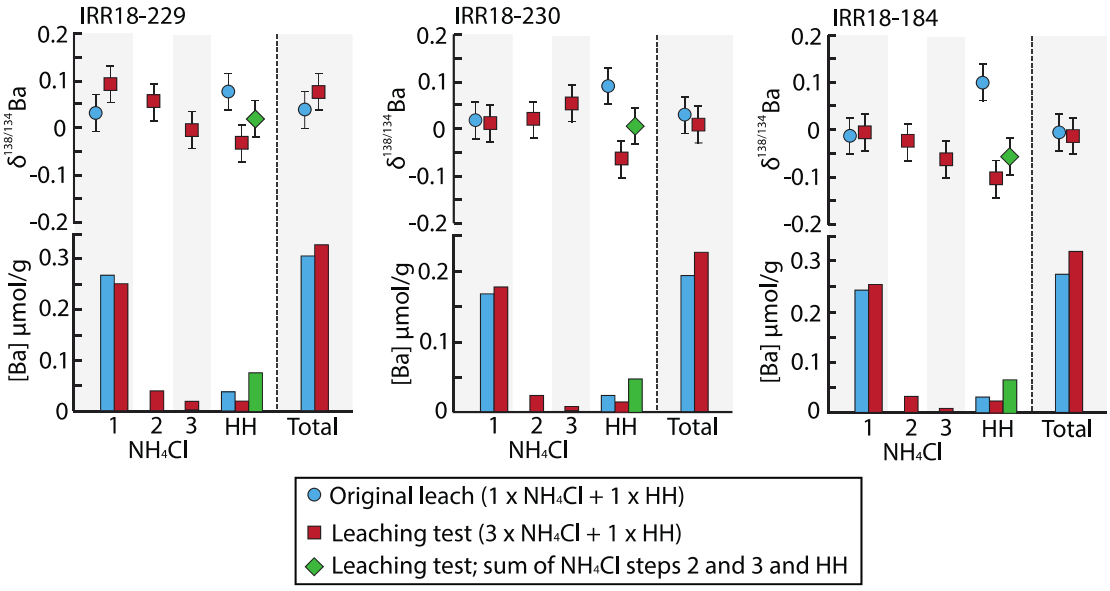

Supplementary Figure 3, Comparison of Ba concentration and $\delta^{138/134}Ba$ results for procedures employing 1 x 1M NH_4Cl versus 3 x 1M NH_4Cl steps.

The 1.7M acetic acid and 1M HCl steps of the leaching procedure (steps 3 and 4; Supplementary Table 2) are intended to target carbonate phases. The 1.7M acetic acid step (step 3) contains the lowest Ba content of all the leaching steps, amounting to 0.5 % (median fraction) of the total Ba pool of the river sediments (Figure 4; main article). The 1M HCl step (step 4) have higher Ba contents, amounting to 3.5% (median fraction) of the total Ba pool of the river sediment. It is possible (and in fact likely) that these steps leach Ba from non-carbonate phases, especially the more

aggressive 1M HCl step. As evidence of this, Ba correlates with Al in these leachates (Al being a tracer of silicate mineral leaching) (Supplementary Fig. 4). The Ba/Al ratios of the1M HCl steps are similar to those of the residue digestion step (step 5; targeting silicates, Supplementary Table 1). Based on this, the Ba contents of the 1M HCl step are interpreted to be dominated by leaching of silicate phases. The 1.7M acetic acid leachates likely give a more accurate assessment of the Ba contents of carbonate phases within the riverine sediments.

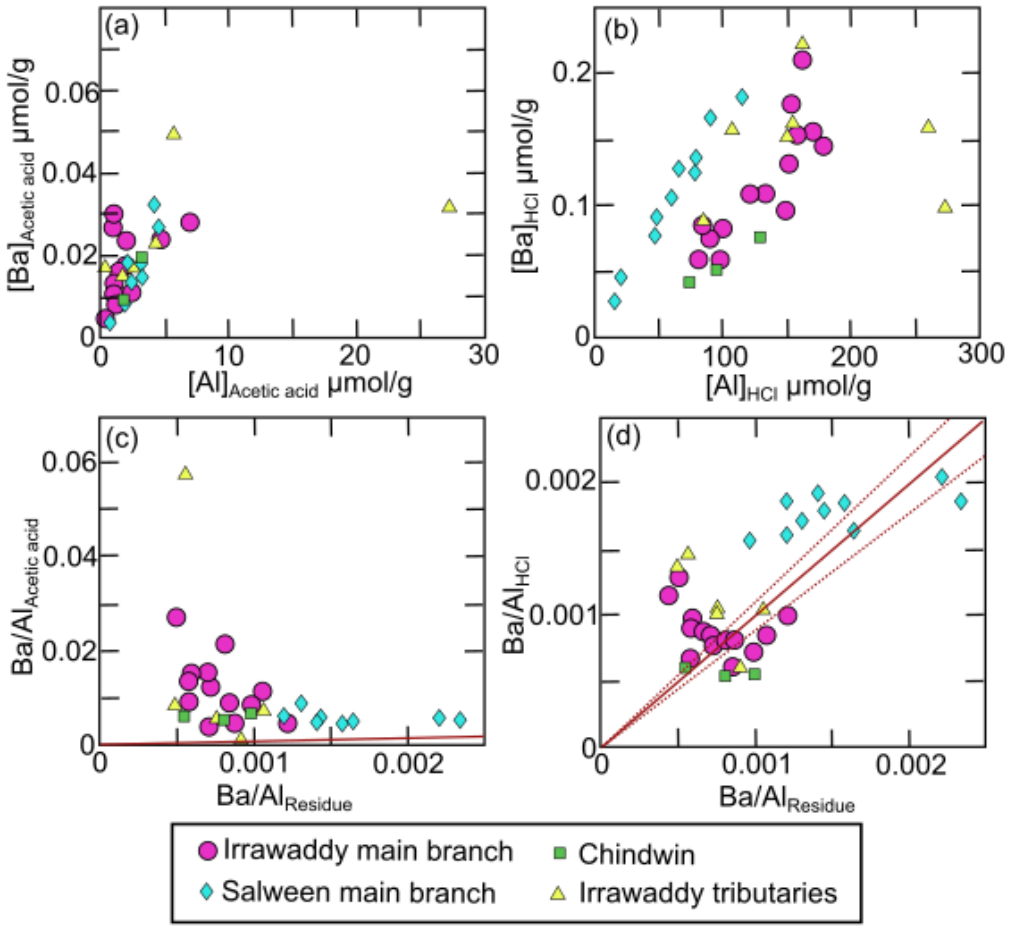

Supplementary Fig. 4, Comparison of Ba and Al in the 1.7M acetic acid (step 3) and 1M HCl (step 4) leachates. Solid red lines in panels (c) and (d) show 1:1 relationships with dashed red lines showing 10% intervals.

S.3 Details of the analytical methods for Ba isotope measurements

S.3.1. Sample preparation protocols

Aliquots of acidified river water and leachate solutions containing ~200 ng of Ba were weighed and equilibrated with a known quantity of the ^{130}Ba-^{135}Ba double spike solution to achieve a molar spike/sample ratio of 0.2. Spiked river water aliquots were then evaporated to dryness and refluxed with 1ml of aqua regia (0.85ml 10M HCl + 0.15 16M HNO_3) to oxidize any organics. Spiked aliquots of 1M NH_4Cl, 5mM HH and 1.7M acetic acid leaching solutions were evaporated to dryness before refluxing and evaporation of 1ml of aqua regia 3 times. Multiple aqua regia steps were found to be necessary to fully oxidize NH_4 ions, which inhibited Ba ionization during TIMS measurements. Spiked aliquots of lithium borate fusion solutions were evaporated to dryness. Dried residues were then heated at 80°C to 120°C for 48 to 72 hours to sublimate the borate salt. Following these treatments, sample residues were converted to chloride form by refluxing and evaporation of 1ml 6M HCl, prior to dissolution in 1ml 3M HCl ready for loading onto cation exchange columns.

Barium was purified from the sample matrices using a two-stage cation exchange chromatography procedure adapted from previous studies (Hsieh and Henderson, 2017). Details of this procedure are given in Supplementary Table 4 and results of the calibration of this procedure shown in Supplementary Figure 5. Final Ba elution solutions were evaporated to dryness and organics leached from the cation exchange resin were subsequently oxidized by repeated treatment with 16M HNO_3, followed by 6M HCl to convert to Cl form prior to isotopic analyses using TIMS. The procedural blank was between 0.01 and 0.67 ng (n=7) representing <0.33 % of the Ba

processed in the samples. This level of blank was too low for determination of its isotope composition and was deemed negligible, so that no blank corrections were applied to the data.

Supplementary Table 4, Two stage cation exchange chromatography procedure used to purify Ba from sample matrices prior to isotopic analyses

First stage: using 1ml of AG50-X8 resin (200-400 mesh) in a Teflon shrink fit column with as aspect ratio of 0.1 (diameter:length)	
Step	**Reagent**
Clean resin	10 ml milli-q H_2O 10 ml 6M HCl
Condition resin	10 ml 3M HCl
Load sample	In 1ml 3M HCl
Elute matrix	7 ml 3M HCl
Elute Ba	3ml 4M HNO_3
Second stage: using 0.2ml of AG50-X8 resin (200-400 mesh) in a Teflon shrink fit column with as aspect ratio of 0.1 (diameter:length)	
Step	**Reagent**
Clean resin	2 ml milli-q H_2O 2 ml 6M HCl
Condition resin	2 ml 3M HCl
Load sample	In 0.2 ml 3M HCl
Elute matrix	1.4 ml 3M HCl
Elute Ba	0.6 ml 4M HNO_3

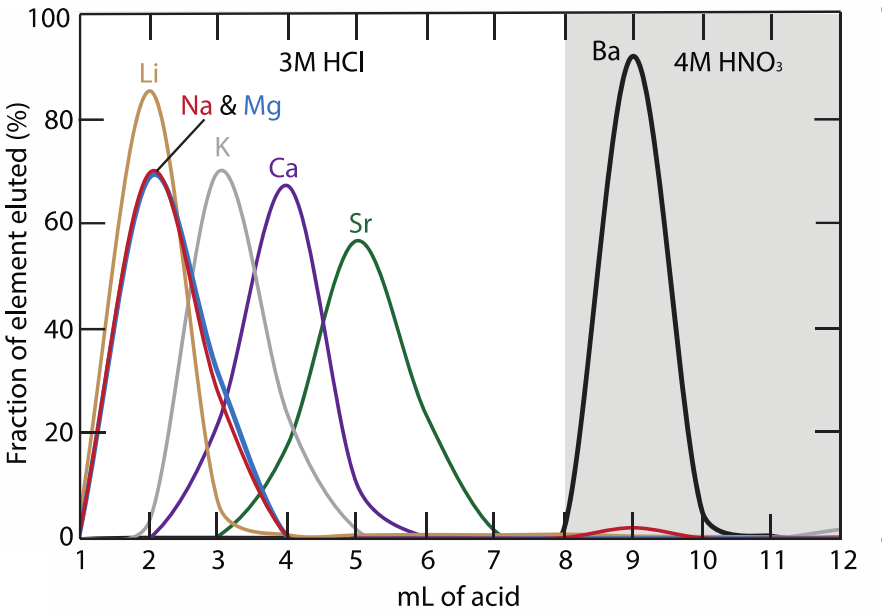

Supplementary Figure 5, Calibration results for the cation exchange chromatography procedure used to purify Ba from sample matrices prior to isotopic analyses.

S.3.2. Barium isotope measurement protocols

Barium isotope analyses using TIMS employed a double Re filament assembly (99.999% purity zone refined; HCROSS), with Ba loaded onto the evaporation filament in chloride form. Barium ionization was achieved by applying currents of 2000 to 2500 mA to the ionization filament and 50 to 500 mA to the evaporation filament. During an analysis, the ion beam intensities at atomic masses 130 (Ba), 134 (Ba), 135 (Ba), 136 (Ba), 137 (Ba) and 138 (Ba) were simultaneously monitored using Faraday cups equipped with 10^{11} Ω resistors. Typical ion beam intensities for ^{138}Ba were ~5 to 10 V. Analyses consisted of 30 blocks of 10 integrations of 8.389 seconds. An electronic baseline was measured prior to each measurement block and was subtracted from the signal.

1768 Interferences from La and Ce (^{138}Ce on ^{138}Ba and ^{138}La on ^{138}Ba) were
1769 checked at the start of analyses by switching the magnet to focus ^{139}La and ^{140}Ce into
1770 the central Faraday Cup. They were also checked periodically throughout analyses
1771 that required higher than typical filament currents (see below). For the vast majority
1772 of analyses no ^{139}La or ^{140}Ce signal was detected. For a small number of analyses (11
1773 out of 85), ^{140}Ce beams of up to 5mV (but typically <1 mV) were observed. These
1774 corresponded to samples requiring higher filament currents (>2700 mA and 500 mA
1775 on the ionization and evaporation filaments respectively) to achieve the desired Ba ion
1776 beam intensities (~5 to 10 V on ^{138}Ba). This level of ^{138}Ce interference corresponds to
1777 <0.001 % of the ^{138}Ba beam, shifting the measured $\delta^{138/134}$Ba values by less than the
1778 internal error of the measurements (typically 0.01‰). These inference levels were
1779 deemed negligible and therefore no corrections were applied to the data.
1780 The $\delta^{138/134}$Ba values (eqn. 11; main article) were calculated offline following
1781 the inversion scheme outlined by Rudge et al. (2009) using the isotopes ^{130}Ba, ^{134}Ba,
1782 ^{135}Ba and ^{138}Ba. Barium concentrations were determined by isotope dilution.
1783
1784 *S.3.3. Accuracy and precision of barium isotope analyses*
1785
1786 The SRM's NIST3104a and NBS-127 were analyzed multiple times during
1787 each measurement session. Over the course of the study (spanning 18 months)
1788 $\delta^{138/134}$Ba values for NIST3104a systematically drifted by -0.05 ‰. To correct for this
1789 instrumental drift, data were grouped into blocks each spanning several weeks to
1790 months, and were corrected relative to the average NIST3104a measured during that
1791 time period. Analyses of the secondary Ba standard NBS-127 corrected for
1792 instrumental drift over the course of the study yielded $\delta^{138/134}$Ba = -0.30 ± 0.04 ‰

(mean ± 2SD, n = 31). This value agrees within uncertainty of those reported by other laboratories (-0.28 ‰; mean of values reported by Horner et al., 2017, Geymann et al, 2019, Tian et al., 2019, Tieman et al., 2020, Bridgestock et al., 2021) validating the accuracy of the method. The long-term reproducibility of these drift corrected NBS-127 are taken to represent the uncertainty of the data. This level of uncertainty (± 0.04 ‰; 2SD) is significantly larger than the typical internal error of the individual measurements (± 0.01 to 0.02 ‰; 2SE). We suspect that this difference is due to degradation of the Faraday cups. Eight out of 85 sample analyses yielded internal errors (2SE) higher than ± 0.04 ‰ due to poor ion beam intensities. The internal errors are quoted as the uncertainty for these samples.

The reproducibility of the data was further assessed by repeat measurements of the geological SRM BCR-2 ($\delta^{138/134}$Ba = 0.07 ± 0.01 ‰; mean ± 2SD, n = 3) and an in house standard '50% Highland Spring' ($\delta^{138/134}$Ba = 0.13 ± 0.05 ‰; mean ± 2SD, n = 5). The latter in house standard was made from the commercially available Highland Spring mineral water, which was diluted by 50% using milli-q water and acidified to pH < 2 using 16M HNO_3 (Knight et al., 2024). It was selected to have a similar matrix to river water. Aliquots are available for measurement by other laboratories upon request to the authors. Alongside BCR-2, single measurements of $\delta^{138/134}$Ba values the geological SRM's AGV-2 (0.10 ‰), JB-2 (0.06 ‰) and BHVO-2 (0.07 ‰) were conducted, with results agreeing within uncertainty of those reported by other laboratories (Supplementary Fig. 6). 50% Highland Spring was processed through the same sample preparation procedure as described for filtered river water samples. The geological SRMs were digested in 16M HNO3 – 28M HF mixtures, prior to processing through the sample preparation and measurement procedures outlined above.

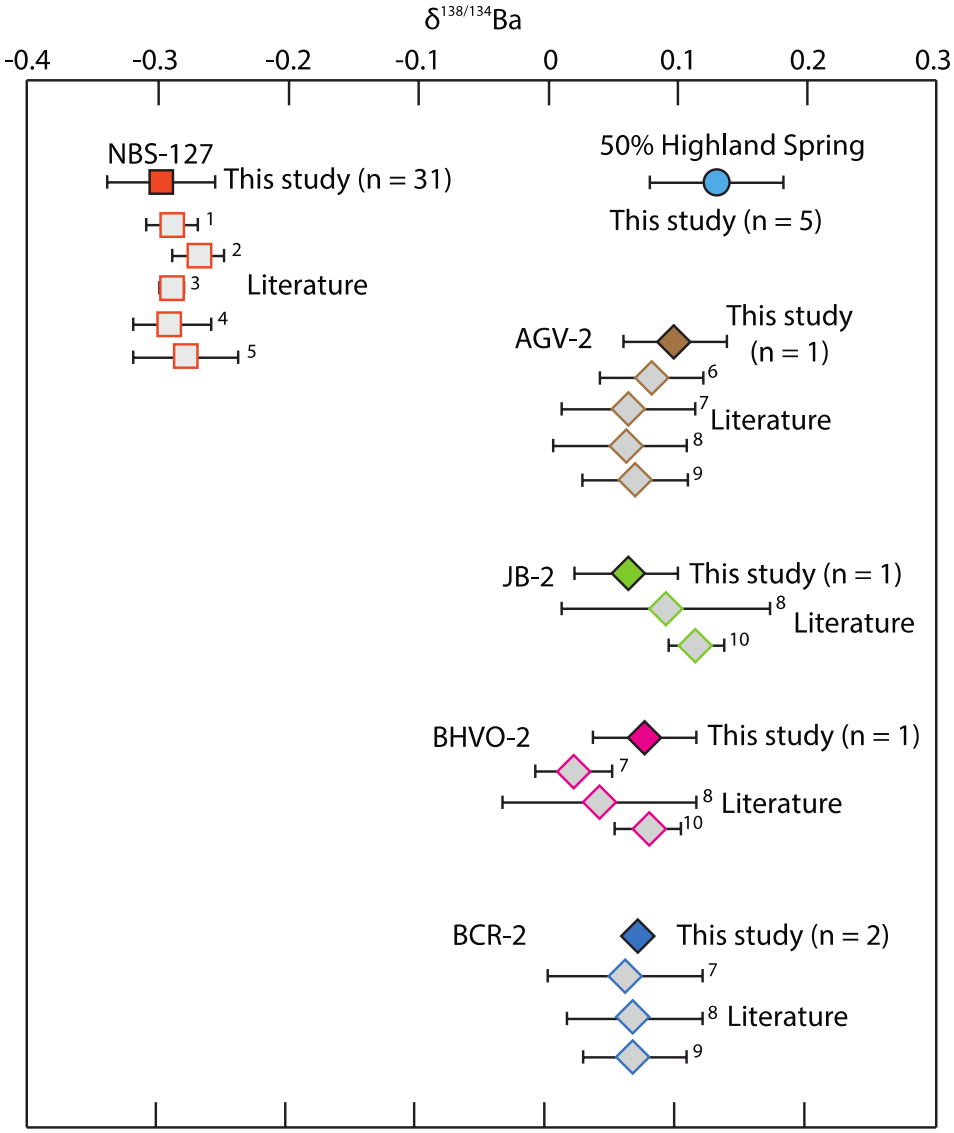

Supplementary Fig. 6, Comparison of standard reference material $\delta^{138/134}$Ba values determined in this study to other laboratories. [1]Bridgestock et al., 2021, [2]Horner et al., 2017, [3]Geymann et al, 2019, [4]Tieman et al., 2020, [5]Tian et al., 2019, van Zuilen et al., 2016[6], An et al., 2020[7], Nan et al., 2015[8], Nan et al., 2018[9], Miyazaki et al., 2014[10].

Barium concentrations determined by isotope dilution using the TIMS isotopic data agree within 10% of those determined by ICP-OES for the majority of samples (Supplementary Fig. 7). The Ba concentration obtained by isotope dissolution from

repeat isotopic analyses of the internal standard '50% Highland Spring' yielded 1677 ± 45 nmol/kg (mean ± 2SD, 2RSD = 2.7%, n = 5).

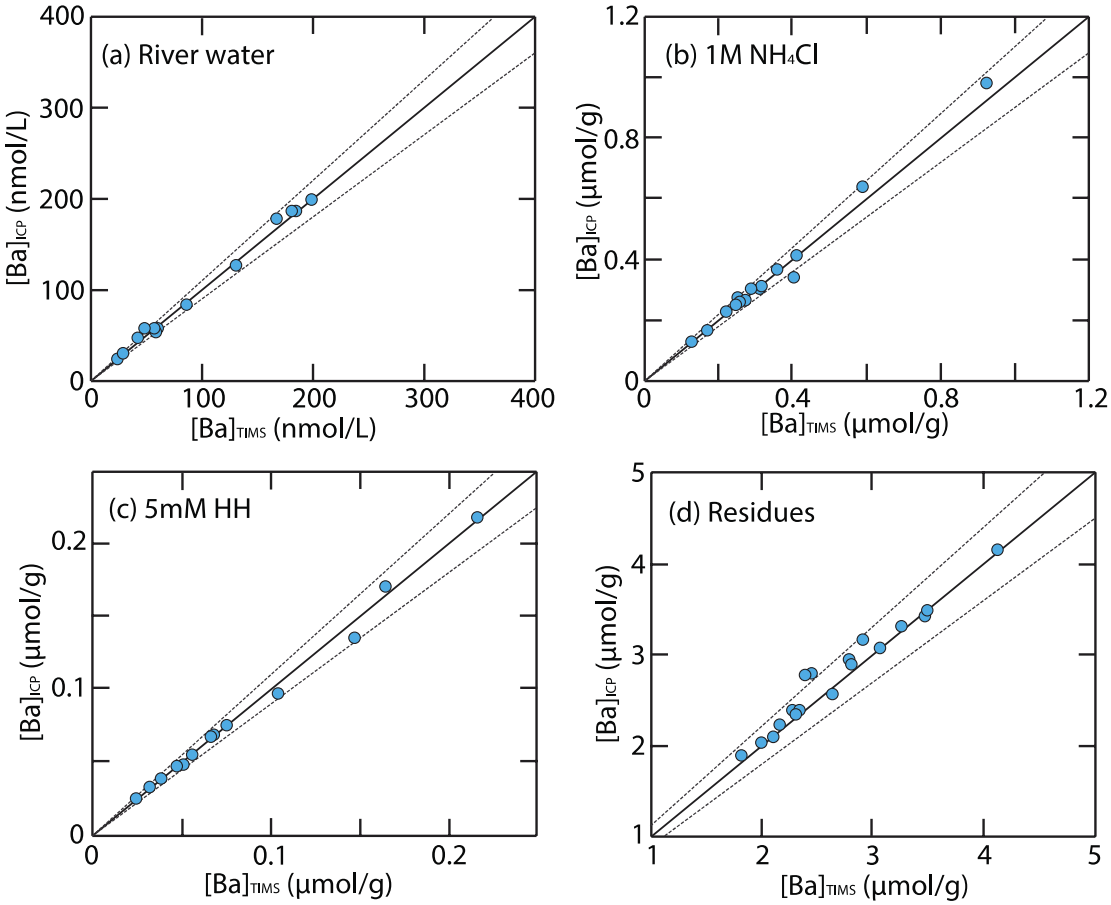

Supplementary Fig. 7, Comparison of Ba concentrations determined by ICP-OES (ICP) and isotope dilution using the TIMS isotopic data (TIMS) for (a) river waters, (b) 1M NH4Cl sediment leachates, (c) 5mM sediment leachates and (d) total digestions of sediment residues. Solid black lines denote 1:1 relationship and dashed lines ± 10% intervals.

S.4. Rain sample results

Dissolved Ba concentrations in the rain samples positively correlate with both Cl and Al, representing tracers of seasalt and mineral dust components of atmospheric

aerosols (Supplementary Fig. 8). The Ba/Cl ratios of the rain samples however are ~12,000 times higher than that of seawater, which rules out seasalt as an important source of the Ba in the rain samples. The Ba/Al ratios of the rain samples are closer that that over the upper continental crust, representing the approximate expected composition of mineral dust, although are 13 to 83 times higher. We interpret this data to reflect that dissolution of mineral dust is the principal source of Ba in the rain samples, with the relative enrichment of Ba over Al reflecting the higher solubility of Ba compared to Al.

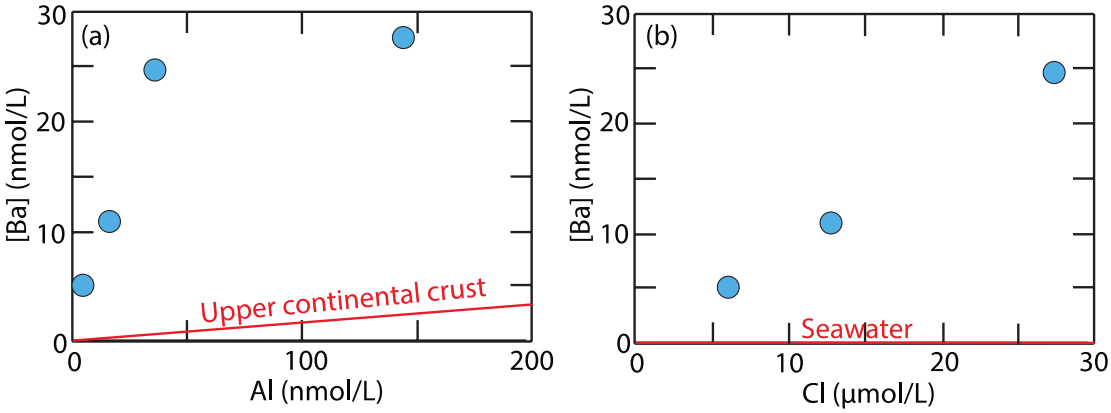

Supplementary Fig. 8, Dissolved Ba, Al and Cl concentrations of rain water samples collected in the Irrawaddy and Salween river catchments. The red line in panel (a) shows the Ba/Al ratio of the upper continental crust of 0.0015 mol/mol (Rudnick and Gao, 2003), while that in panel (b) shows the Ba/Cl ratio of seawater of 7.32×10^{-8} mol/mol. Note that of the 5 rain waters collected, Al was below the limits of detection in 1 sample, while only 3 were measured for Cl concentrations.

S.5 Suspended particulate material depth profiles for Pyay and Hpa An

Suspended particulate material concentrations and grain size (D_{50}) increase with channel water depth (Supplementary Fig. 9). This heterogeneity in SPM

concentrations is an important consideration for constraining channel integrated f_{diss} (and hence $\delta^{138/134}Ba_{out}$) during a given sampling period. However, $[Ba]_{sp}$ decreases with grain size (Fig. 5; main article) compensating for the effects of vertical variations in SPM concentration on f_{diss}.

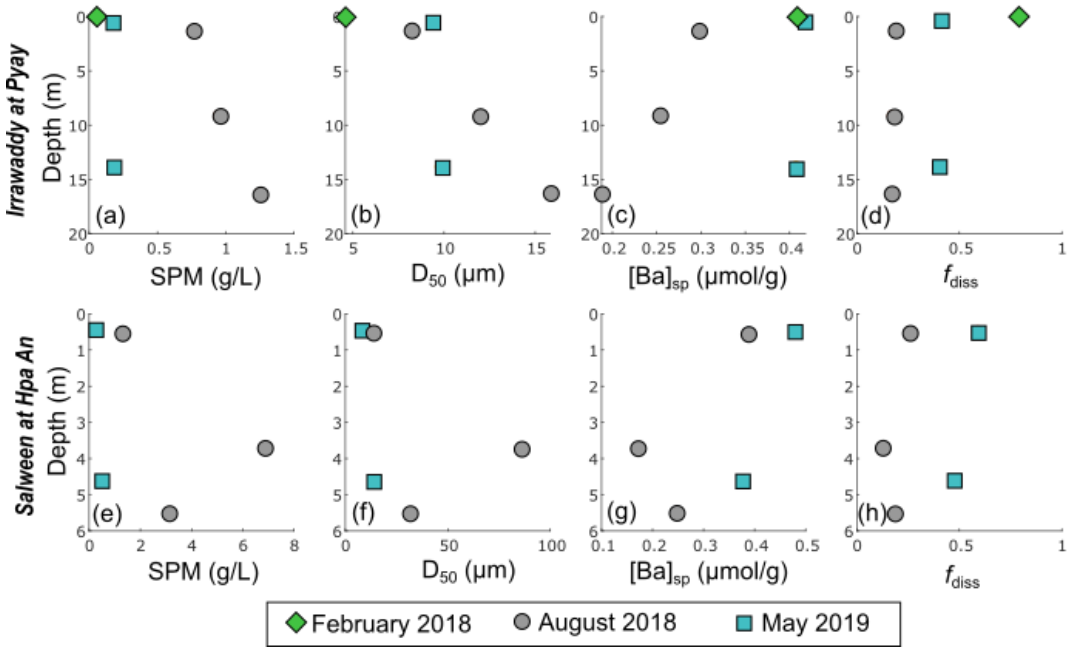

Supplementary Figure 9, Depth profiles of SPM concentrations and compositions sampled at Pyay (Irrawaddy River; panels a to d) and Hpa An (Salween River: panels e to f) under different hydrological conditions.

References

An, Y-J., Li, X. and Zhang, Z-F., 2020, Barium isotopic compositions in thirty-four geological reference materials analysed by MC-ICP-MS, *Geostandards and geoanalytical research*, 44, 183-199, doi:10.1111/ggr.12299

Bridgestock, L., Nathan, J., Paver, R., Hsieh, Y-T., Porcelli, D., Tanzil, J., Holdship, P., Carrasco, G., Annammala, K. V., Swarzenski, P. W. and Henderson, G. M., 2021, Estuarine processes modify the isotope composition of dissolved riverine barium fluxes to the ocean, *Chemical Geology,* 579, 120340, doi:10.1016/j.chemgeo.2021.120340

Geymann B. M., Ptacek J. L., LaVigne M. and Horner T. J., 2019, Barium in deep-sea bamboo corals: Phase associations, barium isotopes, and prospects for

paleoceanography, *Earth and Planetary Science Letters*, 525, 115751, doi:10.1016/j.epsl.2019.115751

Horner T. J., Pryer H. V., Nielsen S. G., Crockford P. W., Gauglitz J. M., Wing B. A. and Ricketts R. D., 2017, Pelagic barite precipitation at micromolar ambient sulfate, *Nature Communications*, 8, 1242, doi:10.1038/s41467-017-01229-5

Hsieh Y-T. and Henderson G. M., 2017, Barium stable isotopes in the global ocean: Tracer of Ba inputs and utilization, *Earth and Planetary Science Letters*, 473, 269-278, doi:10.1016/j.epsl.2017.06.024

Knight, A. C. G., Tipper, E. T. Tipper, Bradbury, H. J., Turchyn, A. V., Andermann, C., Freymuth, H., Elliott, T., Bridgestock, L., 2024, Experimental constraints on barium isotope fractionation during adsorption–desorption reactions: Implications for weathering and erosion tracer applications, Geochimica et Cosmochimica Acta, 384, 194-212, doi:10.1016/j.gca.2024.08.016

Larkin, C. S., Piotrowski, A. M., Hindshaw, R. S., Bayon, G., Hilton, R. G., Baronas, J. J., Dellinger, M., Wang, R., Tipper, E. T., 2021, Constraints on the source of reactive phases in sediment from a major Arctic river using neodymium isotopes, Earth and Planetary Science Letters, 565, 116933, doi:10.1016/j.epsl.2021.116933

Miyazaki T., Kimura J-I. and Chang Q., 2014, Analysis of stable isotope ratios of Ba by double spike standard-sample bracketing using multiple-collector inductively coupled plasma mass spectrometry, *J. Anal. At. Spectrom.,* 29, 483-490, doi:10.1039/c3ja50311a

Nan. X., Wu, F., Zhang, Z., Hou, Z., Haung, F. and Yu, H., 2015, High-precision barium isotope measurements by MC-ICP-MS, *J. Anal. At. Spectrom.,* doi:10.1039/c5ja00166h

Nan X-Y, Yu H-M., Rudnick R. L., Gaschnig R. M., Xu J., Li W-Y., Zhang Q., Jin Z-D, Li X-H. and Huang F., 2018, Barium isotopic composition of the upper continental crust, *Geochimica and Cosmochimica Acta*, 233, 33-49, doi:10.1016/j.gca.2018.05.004

Rudge, J. F., Reynolds, B. C. and Bourdon, B., The double spike toolbox, 2009, Chemical Geology, 265, 420-431, doi:10.1016/j.chemgeo.2009.05.010

Tian, L-L., Zeng, Z., Nan, X-Y., Yu, H-M. and Haung, F., 2019, Determining Ba isotopes of barite using the Na_2CO_3 exchange reaction and double-spike method by MC-ICP-MS, *J. Anal. At. Spectrom.,* 34, 1459, doi:10.1039/c9ja00064j

Tieman Z. G., Stewart B. W., Capo R. C., Phan T., Lopano C. and Hakala J. A., 2020, Barium isotopes track the source of dissolved solids in produced water from the unconventional Marcellus shale gas play, *Environmental Science and Technology,* 54**,** 4275-4285, doi:10.1021/acs.est.0c00102

Tipper, E. T., Stevenson, E. I., Alcock, V., Knight, A. C., Baronas, J. J., Hilton, R. G., Bickle, M. J., Larkin, C. S., Feng, L., Relph, K. E. and Hughes, G., 2021, Global silicate weathering flux overestimated because of sediment–water cation exchange. *Proceedings of the National Academy of Sciences*, *118*(1), e2016430118, doi:10.1073/pnas.2016430118

van Zuilen K., Nagler T. F. and Bullen T. D., 2016, Barium isotopic compositions of geological reference materials, *Geostandards and Geoanalytical Research*,40, 543-558, doi:10.1111/ggr.12122